1   **Towards an End-to-End Analysis and Prediction System for Weather, Climate, and**

2   **Marine Applications in the Red Sea**

3

4   Ibrahim Hoteit[1,*], Yasser Abualnaja[1], Shehzad Afzal[1], Boujemaa Ait-El-Fquih[1], Triantaphyllos

5   Akylas[2], Charls Antony[1], Clint Dawson[3], Khaled Asfahani[4], Robert J. Brewin[5], Luigi Cavaleri[6],

6   Ivana Cerovecki[7], Bruce Cornuelle[7], Srinivas Desamsetti[8], Raju Attada[1], Hari Dasari[1], Jose

7   Sanchez-Garrido[9], Lily Genevier[1], Mohamad El Gharamti[10], John A. Gittings[1], Elamurugu

8   Gokul[1], Ganesh Gopalakrishnan[7], Daquan Guo[1], Bilel Hadri[1], Markus Hadwiger[1], Mohammed

9   Abed Hammoud[1], Myrl Hendershott[7], Mohamad Hittawe[1], Ashok Karumuri[11], Omar Knio[1],

10   Armin Köhl[12], Samuel Kortas[1], George Krokos[1], Ravi Kunchala[13], Leila Issa[14], Issam Lakkis[15],

11   Sabique Langodan[1], Pierre Lermusiaux[2], Thang Luong[1], Jingyi Ma[1], Olivier Le Maitre[16],

12   Matthew Mazloff[7], Samah El Mohtar[1], Vassilis P. Papadopoulos[17], Trevor Platt[18], Larry Pratt[19],

13   Naila Raboudi[1], Marie-Fanny Racault[18], Dionysios E. Raitsos[20], Shanas Razak[1], Sivareddy

14   Sanikommu[1], Shubha Sathyendranath[18], Sarantis Sofianos[20], Aneesh Subramanian[21], Rui Sun[7],

15   Edriss Titi[22,23], Habib Toye[1], George Triantafyllou[17], Kostas Tsiaras[17], Panagiotis Vasou[1],

16   Yesubabu Viswanadhapalli[24], Yixin Wang[1], Fengchao Yao[1], Peng Zhan[1], George Zodiatis[25]

17

18   [1] King Abdullah University of Science and Technology (KAUST), Thuwal, Saudi Arabia

19   [2] Massachusetts Institute of Technology (MIT), Cambridge, Massachusetts, USA

20   [3] The University of Texas at Austin, Austin, Texas, USA

21   [4] Saudi Aramco, Damam, Saudi Arabia

22   [5] University of Exeter, Cornwall, United Kingdom

---

[*] *Corresponding author*: ibrahim.hoteit@kaust.edu.sa

1

23   [6] Institute of Marine Sciences, Venice, Italy

24   [7] Scripps Institution of Oceanography, La Jolla, California, USA

25   [8] National Center for Medium Range Weather Forecasting (NCMRWF), Noida, India

26   [9] University of Malaga, Spain

27   [10] National Center of Atmospheric Research (NCAR), Boulder, Colorado, USA

28   [11] University of Hyderabad, Hyderabad, India

29   [12] University of Hamburg, Hamburg, Germany

30   [13] Indian Institute of Technology, Delhi, India

31   [14] Lebanese American University, Beirut, Lebanon

32   [15] American University of Beirut, Beirut, Lebanon

33   [16] Ecole Polytechnique, Palaiseau, France

34   [17] Hellenic Centre for Marine Research (HCMR), Anavissos, Greece

35   [18] Plymouth Marine Laboratory (PML), Plymouth, United Kingdom

36   [19] Woods Hole Oceanographic Institution (WHOI), Woods Hole, Massachusetts, USA

37   [20] National and Kapodistrian University of Athens, Athens, Greece

38   [21] University of Colorado, Boulder, Colorado, USA

39   [22] University of Cambridge, Cambridge, United Kingdom

40   [23]Texas A&M University, College Station, Texas, USA

41   [24] National Atmospheric Research Laboratories (NARL), Gadanki, India

42   [25] Coastal & Marine Research Laboratory, Crete, Greece
43

44

45
46
47

2

48 **Capsule Summary**

49 An integrated, high resolution, data-driven regional modeling system has been recently developed

50 for the Red Sea region and is being used for research and various environmental applications.

51

52 **Abstract**

53 The Red Sea, home to the second-longest coral reef system in the world, is a vital resource for the

54 Kingdom of Saudi Arabia. The Red Sea provides 90% of the Kingdom's potable water by

55 desalinization, supporting tourism, shipping, aquaculture and fishing industries, which together

56 contribute about 10-20% of the country's GDP. All these activities, and those elsewhere in the Red

57 Sea region, critically depend on oceanic and atmospheric conditions.

58   At a time of mega-development projects along the Red Sea coast, and global warming,

59 authorities are working on optimizing the harnessing of environmental resources, including

60 renewable energy, rainwater harvesting, etc. All these require high-resolution weather and climate

61 information. Toward this end, we have undertaken a multi-pronged R&D activity in which we are

62 developing an integrated data-driven regional coupled modeling system. The telescopically-nested

63 components include 5km-600m resolution atmospheric models to address weather and climate

64 challenges, 4km-50m resolution ocean models with regional and coastal configurations to simulate

65 and predict the general and mesoscale circulation; 4km-100m ecosystem models to simulate the

66 biogeochemistry; and 1km-50m resolution wave models. In addition, a complementary

67 probabilistic transport modeling system predicts dispersion of contaminant plumes, oil-spill, and

68 marine ecosystem connectivity. Advanced ensemble data assimilation capabilities have also been

69 implemented for accurate forecasting.

3

70   Resulting achievements include significant advancement in our understanding of the

71   regional circulation and its connection to the global climate, development and validation of long-

72   term Red Sea regional atmospheric-oceanic-wave reanalyses, and forecasting capacities. These

73   products are being extensively used by academia/government/industry in various weather and

74   marine studies and operations, environmental policies, renewable energy applications, impact

75   assessment, flood-forecasting, etc.

76

77

78

79   1. **Introduction**

80   The Red Sea is a semi-enclosed, elongated marginal sea, lying between Africa and Asia, connected

81   to the Indian Ocean through the Strait of BaM in the south and to the Mediterranean through the

82   Suez Canal in the north (Fig.1). As a vital resource for fisheries, agriculture, tourism, freshwater

83   through desalination, and a major shipping route, the Red Sea is of paramount political and

84   economic importance for both the region and the world. Influenced by distinct geological,

85   atmospheric, and hydrographic conditions, the Red Sea is a unique LME characterized by the

86   second longest and third largest coral reef system in the world, thriving under one of the warmest

87   and most saline conditions of the world oceans (Edwards and Head 1986). All major

88   oceanographic processes occur in the Red Sea, but at much smaller spatio-temporal scales

89   compared to the global ocean, making it an ideal test basin for studies of climate impact on regional

90   ocean circulations as it is expected to exhibit a faster response to global climate variations (Belkin

91   2009; Carvalho et al. 2018). Despite its political, economic and scientific importance, the Red Sea

92   remains a vastly under-explored region.

93   The Red Sea is a geologically young ocean with an average width of 280 km, length of

94   2000 km, and maximum depths exceeding 2500 m along its axial trench. Extending from 12.5 ºN

95   to 30 ºN in the NW-SE direction, it has a constricted connection with the Gulf of Aden, with a

96   maximum depth of only 137 m at the Hanish Sill. The bathymetry varies from extensive shallow

97   shelves with depths < 50 m in the south to steep-sloped basins with depths > 800 m in the north.

98   The atmospheric conditions over the Red Sea are mainly influenced by the arid surrounding

99   terrestrial environment, the seasonal Indian monsoon system and the orographic effects of the

100 coastal mountains, with the resultant atmospheric forcing exhibiting marked variability on various

101 time scales (Viswanadhapalli et al. 2017). As a result of the arid climate, the annual mean net

102   freshwater loss due to excess of evaporation over precipitation is estimated at ~2 m yr^{-1}, and the

103   heat flux has a relatively small annual mean heat loss of 11 W m^{-2}, but a large annual cycle with

104   a range of ~200 W m^{-2}. Channeled by the coastal mountains, the surface winds tend to follow the

105   direction of the axis of the Red Sea. In summer (June to September) they generally blow from

106   North-West throughout the whole basin, whereas in winter they reverse from South-East to North-

107   West in the southern Red Sea, creating a convergence zone around 18 °N (Langodan et al. 2014,

108   2017a). On smaller spatial scales, intense across-basin winds flowing between the coastal

109   mountain gaps are also observed, the most prominent of which is the Tokar jet at around 18 °N of

110   the African coast. This jet is known to generate surface eddies in the Red Sea (Zhai and Bower

111   2013; Zhan et al. 2018) and to gather moisture from the surface of the Red Sea that can contribute

112   to precipitation over Saudi Arabia and the African Highlands region (Davis et. al. 2017; Dasari et

113   al. 2017). North of 20 °N, the mountain-gap winds usually originate from the Arabian subcontinent

114   and blow westward.

115   In response to the atmospheric forcing and limited exchanges with the Indian Ocean (Pratt

116   et al. 2000), the Red Sea acts as a concentration basin, producing one of the world's saltiest water

117   masses through a complex two-layer overturning system (Fig.2). In annual mean, an overturning

118   cell occupies the upper layer around the sill depth in the south and deepens to about 300 m in the

119   north. It is composed of a northward surface inflow from the Gulf of Aden and an intermediate

120   southward flow (Sofianos and Johns 2007). This layer is directly subject to the annual cycle of

121   surface heat flux and freshwater loss, resulting in marked seasonal surface temperature variations

122   and a northward increase in surface salinity (Sofianos and Johns 2015). The Red Sea intermediate

123   water is formed in the north during winter and is exported into the Gulf of Aden through BaM,

124   driving a two-layer water exchange (Sofianos and Johns 2007; Zhai et al. 2015). During summer,

6

125 the above overturning circulation and water exchange in the strait reverse, following the onset of

126 the Indian summer monsoon (Yao et al. 2014a,b). An intermediate water intrusion at depths 50 –

127 100 m is induced from the Gulf of Aden, the mean surface currents change to flow southward, and

128 the water exchange in BaM becomes a three-layer structure with the deep outflow significantly

129 suppressed (Patzert 1974; Smeed 1997). The lower layer of the overturning system, extending to

130 the basin bottom, is occupied by a nearly homogeneous warm (~21.5°C) and highly saline (~40.5

131 psu) water mass, referred to as the RSDW. A deep circulation with a southward bottom flow and

132 an intermediate northward return flow centered around a depth of 500 m is suggested by

133 geochemical tracers and dissolved oxygen gradients (Cember 1988; Eshel et al. 1994).

134   Despite being characterized as an oligotrophic LME, the Red Sea is a region of remarkable

135 biodiversity and endemism and hosts one of the world's largest coral reef ecosystems (Carvalho

136 et al. 2018). The Red Sea ecosystem is strongly influenced by environmental conditions, which

137 modulate it on different levels (Triantafyllou et al. 2014). The Red Sea has been subject to warming

138 trends (Raitsos et al. 2011; Chaidez et al. 2017; Krokos et al. 2019) causing coral reef bleaching

139 events (Cantin et al. 2010; Osman et al. 2018; Genevier et al. 2019) and significantly impacting its

140 productivity (Raitsos et al. 2015; Gittings et al. 2018). The Red Sea ecosystem, with its relatively

141 simply-shaped and semi-enclosed basin, high biodiversity and rich dynamics, provides the

142 scientific community with an accessible and ideal natural laboratory to study the physical-

143 biological interactions on multiple spatial and temporal scales.

144   Until recently, the Red Sea region remained largely underdeveloped. The last decade has,

145 however, witnessed an unprecedented increase in population and an acceleration in residential,

146 commercial and industrial developments along the coast. NEOM, short for the Latin-Arabic term

147 Neo-Mustaqbal, signifying "new future", is a $500bn mega-project that aims at building a fully-

7

148 automated city operating as an independent economic zone in the northwestern part of Saudi

149 Arabia. The RSP is another mega-development along the central Saudi coast and intends to

150 transform the Red Sea coast into a world-class tourist destination, whose blueprint is primarily

151 based on a coastal lagoon with 90-plus pristine islands.

152   Maintaining a sustainable, healthy marine environment is a core objective of these

153 developments and the Saudi authorities. In this context, understanding and forecasting the regional

154 weather through climate variations is essential for a wide variety of high-impact societal needs,

155 including environmental protection and coastal management, mitigating weather extremes and

156 pollution/contamination, exploration and drilling, accidents response, desalination and plant

157 cooling operations, shipping, harbor management and national security operations, management

158 of fisheries and marine aquaculture, water resources, renewable energy, etc. Given the unique

159 structure of the Red Sea basin and surrounding deserts, and the ocean and atmospheric connections

160 to the global circulation, the need for integrated state-of-the-art modeling and supporting datasets

161 is acute.

162   Founded in 2009 and located on the shores of the Red Sea, KAUST acts as a hub of

163 frontline research in the biological, physical and geological aspects of the Red Sea region. For this

164 purpose, KAUST dedicated significant resources for studying the Red Sea and understanding its

165 resources, with the goal of preserving its fragile ecosystem while at the same time supporting the

166 local authorities to exploit its unique resources. In parallel to the on-going hydrographic and

167 ecological observational efforts, and through sustained and strong collaborations with many

168 international organizations, the Red Sea Modeling and Prediction group at KAUST has led the

169 development of a comprehensive and integrated modeling and prediction system to study, monitor

170 and predict the atmospheric and oceanic phenomena of the region. The system is being built by

8

171 integrating models of atmospheric and oceanic circulations, surface wave, air pollution, dust, and

172 marine biogeochemistry, and developing advanced data analytics and visualization capabilities,

173 achieving remarkable progress in the short span of a decade. The modeling system also relies on

174 *in situ* and remotely-sensed observations (detailed in Table 1) for the purpose of validation and

175 data assimilation and provides insights into the systematic relations between the interactions of

176 different components and the management of various applications.

177 An important achievement from this effort is the first high-resolution atmospheric

178 reanalysis for the region from 1980 till present, generated using our assimilative atmospheric

179 modeling system, which is turning out to be critical not only for the Red Sea climate research, but

180 also contributing to Indian monsoon studies. This regional reanalysis is being used to force the

181 various ocean and transport models tuned to the Red Sea environment. Notably, these capabilities

182 are currently being extensively used to support various industrial and governmental developments.

183 This review paper elaborates on our state-of-the-art modeling and forecasting technologies, their

184 applications, achievements in science and contributions to industry. It first provides a detailed

185 description of our integrated data-driven Red Sea Modeling system version 1 (iReds-M1). It then

186 catalogues some of our salient science findings and industrial applications using iReds-M1

187 simulations. It finally lays down our vision for the future development of the system and research

188 directions.

189

190 2. **The Integrated Red Sea Model (iReds-M1)**

9

191   iReds-M1 is a comprehensive system comprising a set of state-of-the-art modeling components

192   for simulating the atmosphere, ocean, waves, transports, and bio-geochemistry (as schematized in

193   Fig.3). In its present form, the WRF model is used to force various ocean and transport models.

194   The regional ocean and wave models, based on the MITgcm and WWIII, were further recently

195   fully coupled with WRF (Sun et al., 2019). These regional models are further used to force

196   transport models and to nest very high-resolution coastal ocean models. The system is

197   implemented on the Shaheen-II Cray XC40 – supercomputer at KAUST, a 36-cabinet Cray

198   composed of 6,174 dual socket compute nodes based on 16 core Intel Xeon E5-2698v3 processors

199   running at 2.3GHz, capable of delivering a theoretical peak of 7.2 PFLOP/s (Hadri et al 2015). A

200   description of the components follows.

201   *2.1 The atmospheric models*

202   WRF is a state-of-the-art mesoscale model offering numerous advanced physics options for

203   simulating atmospheric processes at various scales, providing a robust and flexible platform for

204   assimilation (Skamarock et al. 2019). In various baseline studies, WRF successfully reproduced

205   the mean regional climate of the AP and its interannual variability (Viswanadhapalli et al. 2017).

206   It also accurately delineated the structure and climatology of the monsoon low-level jet and

207   monsoon inversion over the Arabian Sea (Viswanadhapalli et al. 2019). We further used long-term

208   WRF simulations to carry out detailed assessments of renewable energy resources in the AP

209   (Langodan et al. 2016a; Dasari et al. 2019a), and for analyzing extreme events (e.g.

210   Viswanadhapalli et al. 2016).

211   We have implemented WRF in assimilation mode at 5-km resolution using the ECMWF

212   global reanalysis as initial and boundary conditions to generate the first high-resolution regional

213   reanalysis for the region from 1980 till present (Viswanadhapalli et al. 2017; Langodan et al.

10

214   2017a,b). Available satellite and conventional observations in the AP were assimilated (Fig.4).

215   The reanalysis fields are being used to study, for instance, the regional met-ocean conditions (e.g.,

216   Viswanadhapalli et al. 2017, 2019), to provide vital information about the background state of the

217   regional environment (e.g., Dasari et al. 2020), and to force our regional ocean models (e.g.,

218   Langodan et al. 2014, 2016a; Zhan et al. 2019; Krokos et al. 2020).

219   To simulate air parcel trajectories as well as transport, dispersion, chemical transformation,

220   and deposition, we use HYSPLIT (Draxler et al. 1997). HYSPLIT, forced with specially-generated

221   WRF forcing at 600 m resolution, was recently used to investigate the distributions of air pollutant

222   concentrations at sites along the Red Sea coast, including the NEOM and RSP regions (Dasari et

223   al. 2020).

224   *2.2. The ocean models*

225   The regional Red Sea circulation is simulated using a 1 km resolution MITgcm (Marshall et al.

226   1997a,b). The model domain covers the entire Red Sea including the two gulfs (Suez and Aqaba)

227   at the north end, with an open boundary in the Gulf of Aden. The model topography is generated

228   based on the General Bathymetric Chart of the Ocean (Ioc, 2003), updated with available regional

229   data. The eastern open boundary conditions are extracted daily from the global ocean reanalysis

230   GLORYS2. To resolve the different frequencies of water elevation variations (Churchill et al.

231   2018), the normal velocity at the boundary is adjusted to match the volume flux of GLORYS2.

232   The model is forced with hourly high-resolution WRF downscaled fields, including surface wind,

233   air temperature, specific humidity, precipitation, and downward short-wave and long-wave

234   radiation. The Red Sea MITgcm outputs were validated against different datasets and in various

235   settings and applications (Fig.5). These include studying the general and overturning circulation

236   (Yao et al. 2014a,b), mixed layer variations (Krokos et al. 2020), deep water formation events

11

237   (Yao and Hoteit 2018), eddy characteristics (Zhan et al. 2016; 2019), and internal/baroclinic tides

238   (Guo et al. 2018). In addition, the adjoint model of MITgcm is being used to conduct sensitivity

239   studies of quantities-of-interest with respect to the model states and atmospheric forcings (Zhan et

240   al. 2018).

241   WWIII (Tolman 2008) is used to simulate the waves conditions in the Red Sea at 1 km

242   resolution. The model is configured with 33 frequencies, starting from 0.05 Hz and 36 equally

243   spaced directions and the most recent (ST4) physics formulation (Ardhuin et al. 2010). The

244   extensively validated model outputs (Langodan et al. 2014) were analysed to assess the impact of

245   atmospheric data assimilation on wave predictions (Langodan et al. 2016b), to investigate the

246   physical aspects of the unique seasonally opposing wind-wave systems in the central Red Sea

247   (Langodan et al. 2015), to quantify wave energy potentials (Langodan et al. 2016a), and to study

248   the wind-wave climate and its trends (Langodan et al. 2017a,b; 2018; 2020a).

249   Transport phenomena are simulated using CMS, a multi-scale probabilistic model of

250   particle dispersal (Paris et al. 2013). CMS, driven by the MITgcm flow fields, has been

251   successfully implemented to study concentrate discharges (Zhan et al. 2015), biological

252   connectivity among different coral reef complexes at coastal (Nanninga et al. 2015), basin (Raitsos

253   et al. 2017), and cross-basin scales (Wang et al. 2019). Oil spill transport and weathering processes

254   are simulated with the well-established MEDSLIK oil spill, trajectory and pollutant transport

255   prediction model (De Dominicis et al. 2013a,b; http://www.oceanography.ucy.ac.cy/medslik/) as

256   Lagrangian particles transported by ocean currents, wind, and waves, and a stochastic

257   displacement that parameterizes turbulent diffusion (Zodiatis et al. 2019).

258   The marine biogeochemical cycle is simulated using ERSEM (Baretta et al. 1995). ERSEM

259   is a generic comprehensive model that has been successfully implemented across a wide range of

12

260   coastal and open ocean ecosystems (e.g., Petihakis et al. 2002; Collingridge 2012). It is based on

261   a 'functional' group approach, using size as the major biotic group characteristic. The pelagic

262   model food web consists of four phytoplankton groups, bacteria and three zooplankton groups,

263   and is coupled with the associated benthic model that includes the settling of organic detritus into

264   the benthos and diffusional nutrient fluxes out of the sediment. The pelagic variables include

265   particulate and dissolved organic matter, along with dissolved inorganic nutrients, allowing the

266   coupling of biologically-driven carbon dynamics with the chemical dynamics. ERSEM forced

267   with the outputs of our MITgcm and WRF models outputs has been successfully implemented by

268   Triantafyllou et al. (2014) to describe the main seasonal features of the Red Sea ecosystem.

269   To simulate complex coastal processes, we implemented ocean models specifically

270   designed for coastal and engineering applications at very high-resolutions O(10 m). These include

271   (i) the Delft3d model (Deltares 2016) to simulate coastal circulation, including flow induced by

272   tides and wind, and sediment transport, (ii) the shallow-water ADCIRC model (Luettich and

273   Westerink 2004) to simulate water level variations and surges on an unstructured grid that enables

274   resolution of near-shoreline detail, and (iii) the SWAN model (Booji et al. 1999) that is coupled

275   with both Delft3D and ADCIRC and designed for simulating short crested waves in coastal

276   environments. These models are forced with high-resolution downscaled WRF fields and are

277   nested within the regional MITgcm and WWIII models.

278   *2.3. Coupled Ocean-atmosphere modeling*

279   Ocean temperatures over the Red Sea region play an important role in modulating the region's

280   weather and climate (Gimeno et al. 2010; Sun et al. 2019). Furthermore, while most of the AP

281   experiences hot and dry summers, the conditions in coastal regions east of the Red Sea

282   are relatively cooler and humid owing to transported moisture from the Red Sea. SKRIPS is a new

13

283   regional coupled ocean-atmosphere WRF+MITgcm+WWIII system that was developed as part of

284   iReds-M1 to study air-sea feedbacks in the Red Sea region and to build long-term regional

285   forecasting capabilities (Sun et al. 2019). Coupling between these components is based on ESMF

286   (Hill et al. 2004) and the interfaces are implemented according to the NUOPC consortium. This

287   regional coupled model allows for oceanic mixed layer heat and momentum to interact with the

288   atmospheric boundary layer dynamics at the mesoscale and higher resolution. This should

289   reproduce feedbacks that cannot be well-resolved by coarse-resolution global coupled models and

290   are absent in regional uncoupled models. SKRIPS was used to investigate the heatwaves in the

291   Red Sea region on seasonal scales, demonstrating that the evolving ocean temperatures

292   considerably improve the prediction of the amplitude of these heatwaves (Fig.6), particularly in

293   the coastal region (Sun et al. 2019).

294   *2.4   Data assimilation*

295   Assimilation is a process by which a model is constrained towards available observations to obtain

296   improved forecasts/hindcasts (Edwards et al., 2015; Hoteit et al., 2018). Our atmospheric and

297   ocean general circulation models are equipped with state-of-the-art assimilation packages; DART

298   (Hoteit et al., 2013), which comprises advanced ensemble schemes (Anderson et al. 2009) and the

299   adjoint-based ECCO-4DVAR system (Stammer et al. 2002; Hoteit et al., 2006) for MITgcm, and

300   the extensive assimilation package of WRF (Barker, 2012), which also includes DART. We are

301   currently employing a cyclic 3DVAR for assimilation with WRF (Viswanadhapalli et al. 2017)

302   and an ensemble adjustment Kalman filter (EAKF) for MITgcm (Toye et al. 2017, 2018). We have

303   recently further developed the DART-MITgcm system to operate with hybrid ensembles

304   composed of flow-dependent and seasonally-varying static members (Toye et al. 2019) and

305   demonstrated significant improvements when driving the MITgcm with ensembles of forcing and

14

306   physics (Sivareddy et al. 2019). We are currently working on tuning DART for WRF, and on

307   testing newly introduced ensemble assimilation schemes (Hoteit et al. 2015; Raboudi et al. 2018).

308   The system is being further equipped with new efficient techniques for simulating transport

309   phenomena (El-Mohtar et al. 2018) and control of unmanned vehicles (Wang et al. 2017;

310   Albarakati et al. 2019) under the uncertainties described by the ensembles.

311   We assimilate a variety of observations from different networks, including satellite (e.g.

312   Altimeter SSH and AVHRR SST in the ocean, and QuikSCAT and Advanced Scatterometer winds

313   in the atmosphere) and land-based remote sensing (e.g. weather radars), station-based (e.g.

314   oceanic temperature and salinity observations from moored buoys and ships, meteorological

315   observations from synoptic stations and Metar) and freely drifting (e.g., Argo observations in the

316   ocean, and upper-air soundings of Rawinsonde and pilot balloon) in situ observations. Fig.7

317   demonstrates the important improvement achieved after ocean assimilation, with significant

318   reduction in the SST and SSH biases in the Red Sea and Gulf of Aden compared to the model free-

319   run. On average, assimilation reduced the forecast RMSEs by 0.5°C for SST and 3 cm for SSH.

320   The assimilated ocean solution is closer to both SST and SSH observations than the corresponding

321   interpolated level-4 products. An operational system for the Red Sea is currently being developed

322   based on a Hybrid ensemble assimilation scheme as part of a project with Saudi Aramco.

323   *2.5 Visualization and data analytics*

324   Advanced visualization is an integral component of our system to support data analysis tasks for

325   scientists and non-expert users. We have developed a visual analytics application, called

326   RedSeaAtlas (Afzal et al. 2019a), considering the tasks, computational and operational

327   requirements of the variety of simulation models and observational datasets of the Red Sea region.

328   The application provides a suite of visualization tools that can facilitate diverse research tasks

15

329   through interactive visual exploration and analysis of spatio-temporal multivariate data (Fig.8).

330   These include interactive feature selection, spatial and temporal filtering, overview and details-on-

331   demand, and capability to analyze data from disparate data sources (Afzal et al. 2019b).

332   We have also developed an interactive visual analysis framework, called Ovis (Höllt et al.

333   2013, 2014), for interactive exploration and analysis of ensemble data. The core components of

334   this framework are constructed based upon an efficient GPU-based computation and visualization

335   pipeline. We presented two case studies to showcase the effectiveness of this framework; the first

336   investigated the placement planning and operation of off-shore structures related to oil and gas

337   industry, and the second demonstrated the effectiveness of this system to plan pathways of

338   autonomous sea vehicles (gliders) through interactive exploration and analysis of ensemble data

339   (Höllt et al. 2013, 2015).

340

341   **3. iReds Salient Contributions to Science and Industry**

342   *3.1 Study of the Red Sea Region Circulation, Climate and Ecosystem*

343   <u>Atmospheric variability:</u> Motivated by the background knowledge from the analysis of global

344   fields, and to meet the need for high-resolution datasets to resolve mesoscale characteristics, we

345   developed a regional reanalysis at 5 km resolution for a 39-year (1980-2018) period (wind details

346   captured by this regional reanalysis are illustrated in Fig.4). The reanalysis fields accurately

347   reproduced the known regional climatic features such as the Red Sea Trough, Red Sea

348   Convergence Zone, Arabian anti-cyclone, and seasonal circulation patterns (Viswanadhapalli et

349   al. 2017). It has been further extensively used to drive iReds ocean models and for subsequent

350   regional applications, and to support the mega-projects being developed along the Red Sea coast.

351   Several studies were also conducted using convective-permitting WRF configurations to

16

352 investigate the predictability of extreme rainfall over the Mecca region, discussed more in detail

353 below.

354   Based on global reanalyses, our study of the regional surface air temperature suggested that

355 it is strongly modulated by the circulation patterns (Attada et al. 2018a), and demonstrated an

356 impact of the Indian summer monsoon through westward propagating Rossby-waves (Attada et al.

357 2018b). Dasari et al. (2017a, 2019b) showed that the baroclinic instability induced by the

358 intensification and southward shift of the subtropical westerly jet over the AP facilitates an

359 increase in the passage of synoptic-transients and winter rainfall. Kunchala et al. (2018; 2019)

360 showed a significant increasing trend in the recent decade in the summer AOD over AP, related to

361 an intensification of the Tokar jet.

362 <u>Ocean general circulation:</u> The Red Sea MITgcm has provided an unprecedented description of

363 the 3D basin circulation and its seasonal and interannual variability. The local buoyancy forcing

364 and Indian monsoon seasonally reverse the basin overturning circulation, and ultimately modulate

365 the water exchanges with the Gulf of Aden through BaM (Yao et al. 2014a,b). Analysis of the

366 interannual variability of the exchanges based on long-term MITgcm simulations forced with the

367 in house high resolution regional Red Sea reanalysis further demonstrated a strong dependence on

368 the intensity and duration of the Indian monsoon (Raitsos et al. 2015; Dreano et al. 2016; Xie et

369 al. 2019). Such simulations also revealed the episodic nature of deep-water renewal related to

370 specific atmospheric events and provided updated estimates of the deep-water renewal time Yao

371 and Hoteit (2018). A 1 km model simulation together was recently analyzed to provide a detailed

372 description of the seasonal and spatial variability of the Red Sea mixed layers (Krokos et al. 2020).

373 The study revealed the dominant role of the air-sea heat fluxes on the mixed layers seasonal

17

374   variability and the north-south gradient while the effects of extreme evaporation mainly manifest

375   on interannual time scales.

376   MITgcm-ERSEM-CMS simulations, combined with various remote sensing datasets, have

377   provided new insights into the manner in which physical drivers such as buoyancy fluxes and

378   ocean mixing, and biogeochemical processes drive the ecosystem in the Red Sea. Despite a limited

379   supply of nutrients, their subsurface intrusion from the Gulf of Aden and the winter deep

380   convection drive elevated values of primary productivity in the south during summer (Raitsos et

381   al. 2013; Dreano et al. 2016) and in the north during winter (Gittings et al. 2018). Moreover, marine

382   larvae/planulae disperse nearly passively with the circulation, forming a homogenous genetic

383   connectivity across geographically separated reef sites within most of the basin (Fig.9; Raitsos et

384   al. 2017), except for the southern Red Sea which was suggested to be physically connected with

385   the Indian Ocean (Wang et al. 2019).

386   Mesoscale circulation: The upper-layer Red Sea circulation is characterized by complex and highly

387   varying mesoscale activity, consisting of energetic semi-permanent and transient eddies, with

388   stronger activity during winter (Zhan et al. 2014). Spatially, the central and northern regions show

389   annual eddy kinetic energy (EKE) peaks during both seasons, with effects on the water column

390   reaching down to 300 m and intensified towards the surface. The MITgcm outputs suggested that

391   the northward gradient of heat loss tilts the isopycnals, which gradually deepen towards the north,

392   thereby enabling baroclinic instabilities and hence the eddy generation (Zhan et al. 2016). The

393   EKE dominates the mean flow kinetic energy (Zhan et al. 2016), with the fate of observed eddies

394   being largely governed by atmospheric forcing and local ocean conditions (Zhan et al. 2018).

395   Driven by considerable heat fluxes, intensified eddy activity promotes convection processes,

396   especially during winter in the north (Papadopoulos et al. 2013; 2015). The northward transport of

18

397   warmer and fresher water by eddies reduces the intrinsic meridional gradient and flattens the

398   isopycnals, which in turn limits the eddy generation and was interpreted as a typical negative

399   feedback mechanism (Zhan et al. 2019). Based on WRF-MITgcm-CMS simulations, the Red Sea

400   mesoscale circulation was found to play an important role in transporting biogeochemical tracers

401   within the basin (Fig.9) and in supporting the marine ecosystem (Zhan et al. 2014; Dreano et al.

402   2016; Raitsos et al. 2017; Guo et al., 2020).

403   <u>Tides:</u> The main tidal signal in the Red Sea propagates from the Arabian Sea through BaM.

404   Observations and simulations suggest a high variability of tidal elevation with latitude, with the

405   northern and southern basins exhibiting relatively large amplitudes compared to the central basin

406   (Guo et al. 2016). Barotropic tides generate internal tides and solitary waves, mainly on the steep

407   sides of the deep trough in the southern part of the Red Sea (da Silva et al. 2012; Guo et al. 2016).

408   Our simulations using a 200 m non-hydrostatic MITgcm and CMS showed that the breaking of

409   internal waves induces vertical mixing, which could increase the supply of nutrients to the euphotic

410   zone and enhance biological productivity, by disrupting the pycnocline and inducing turbulence

411   (Guo et al. 2020).

412   <u>Waves:</u> Based on long-term WWIII simulations forced with the in-house WRF downscaled Red

413   Sea reanalysis, the wave variability in the Red Sea was naturally associated with the dominant

414   regional wind regimes (Langodan et al. 2014). Although wind intensity in the basin is usually

415   moderate, a prolonged duration and the existence of a long fetch may give rise to waves that reach

416   up to 3.5 m. The irregular shape of the Red Sea coast creates shadowed areas, especially in the

417   south where southward-moving waves reduce to swell and propagate unidirectionally. During

418   summer, consistent northwesterly winds generate mean wave heights of 1-1.5 m in the north,

419   frequently exceeding 2 m (Langodan et al. 2014, 2018). The southward wave system persists

420   throughout the year, while the northward system associated with the monsoon winds exhibits a

421   well-defined seasonality between October and April (Langodan et al. 2018). The co-existence of

422   northward and southward waves in winter creates a convergence zone in the central Red Sea

423   (Langodan et al. 2015). Various transversal jets, such as the Tokar jet on the Sudan coast and others

424   that originate in the AP generate locally dominant wave regimes (Langodan et al. 2017b). These

425   exhibit strong seasonality and are usually dominated by other systems.

426   Ecological indicators: The recent development of multi-sensor satellite missions, such as the

427   Ocean Colour Climate Change Initiative (OC-CCI, Sathyendranath et al. 2019), has increased the

428   coverage of surface Chl-a measurements in the Red Sea by enhancing the retrieval of satellite data

429   under adverse atmospheric conditions. Using available in-water measurements of Chl-a, Brewin

430   *et al.* (2013, 2019) and Racault *et al.* (2015) have shown that both standard ocean-colour

431   algorithms and the OC-CCI algorithm perform well in the Red Sea, but further improvements have

432   been achieved by developing a regional algorithm specifically-tuned to the basin (Brewin et al.

433   2015).

434   The analysis of the derived long-term Chl-a dataset together with the MITgcm, WRF, CMS

435   and ERSEM simulations has enabled an unprecedent understanding of the general functioning of

436   the Red Sea ecosystem and its productivity. The open waters of the Red Sea Chl-a exhibit a distinct

437   seasonality with maximum concentrations seen during wintertime, which was attributed to vertical

438   mixing in the north and wind-induced horizontal intrusion of nutrient-rich water in the south, and

439   minimum concentrations during summer (Raitsos et al. 2013). However, large sporadic blooms

440   have been reported during summer in the coastal southern Red Sea driven by the GAIW (Racault

441   et al. 2015; Dreano et al. 2016). The concentration and the duration of the phytoplankton growing

442   season in the Red Sea are modulated by the strength of the winter monsoon over the Arabian Sea,

20

443   which affects the horizontal advection of fertile waters from the Indian Ocean (Raitsos et al.

444   2015). Warmer conditions over the region were also associated with substantially weaker winter

445   phytoplankton blooms, which initiate later and are shorter in their overall duration (~ 4 weeks)

446   (Gittings et al. 2018; Gittings et al. 2019a). Satellite-derived estimates of phytoplankton size

447   structure are in good agreement with the *in situ* measurements, and also capture the spatial

448   variability related to regional mesoscale dynamics (Gittings et al. 2019b). iReds outputs were also

449   used along with in situ and satellite observations to investigate the basin ecological responses to

450   the combined effects of biogeochemical and physical environmental stressors (Ellis et al., 2019).

451

452   *3.2 High-Resolution Nested Modelling in Support of New Mega-Developments along the Red*

453   *Sea Coast*

454   <u>Met-Ocean modeling in NEOM:</u> NEOM spreads over an area of 26,500 km^2 along the northern

455   Red Sea coast of Saudi Arabia, bordering Jordan and Egypt. To support environmental impact

456   assessment efforts and to generate essential met-ocean data required for initial planning, high-

457   resolution atmospheric and oceanic models were implemented and nested within the regional Red

458   Sea models. A 3-year 600 m resolution WRF simulation was performed to investigate the

459   orographic influence on the coastal atmospheric conditions and to drive high-resolution coastal

460   ocean models. Air-quality was also investigated using HYSPLIT driven by the WRF fields to study

461   dispersion of pollutants and their diurnal variations in relation to the land-sea breezes and boundary

462   layer heights (Dasari et al. 2020).

463   The large-scale ocean circulation of the NEOM region simulated by the regional MITgcm

464   suggests numerous eddy features with the topography being the critical factor driving their

465   interactions. A coupled Delft3D+SWAN model configuration with horizontal resolution of 50 m

21

466   and 10 vertical sigma levels was nested within MITgcm to resolve the coastal circulations and was

467   forced with tides and 600 m WRF fields. Seasonal simulations highlighted different coastal

468   circulation features, including a prominent localized eddy-like structure in the center of the NEOM

469   lagoon where the inner water connects with the open ocean through a narrow channel, and a

470   persistent northwest-southeast current along the broad offshore edge of the coral reefs. The

471   "residence time" estimates based on trajectories of simulated passive particles suggests a faster

472   ventilation rate in winter. The SWAN model nested within the regional WWIII suggested a

473   dominance of locally generated waves in the southeast direction, with a maximum significant wave

474   height of ~0.8 m, associated with consistent strong northwesterlies.

475   Extreme waves and water levels for KAEC: KAEC is a new city under development along the

476   western Saudi coast, comprising the largest port on the Red Sea, residential districts, and an

477   industrial valley. The area is surrounded by coral reefs and includes a shallow lagoon on its

478   southern side. We supported the development of the sea wall for coastal protection by providing

479   estimates of extreme wave heights and water levels for the KAEC shoreline. For this, we used a

480   coupled ADCIRC+SWAN model configured on a triangular grid with an open boundary in the

481   Arabian Sea. The model's unstructured-grid resolution varied from a maximum vertex spacing of

482   approximately 60 km near the boundary down to 60 m near the KAEC coastline. The bathymetry

483   was generated from 0.5 m resolution LiDAR surveys of the KAEC coast. Simulations were carried

484   out for a 30-year period, forced with the our WRF downscaled atmospheric reanalysis. Extreme

485   value analyses were applied to estimate different return levels of wave heights and water levels.

486   The model effectively simulated the dampening of the offshore waves propagating towards the

487   shoreline by the coral reefs (Fig.10). The KAEC coastline being characterized by a weak tidal

488   regime, extreme sea levels are dominated by meteorological activity, mostly observed during

22

489   winter. The 100-year return levels of wave heights and water level were estimated at 70 cm and

490   65 cm, respectively, only marginally (~5 cm) different from the 30-year maxima (Langodan et al.

491   2020b; Antony et al. 2020).

492

493   *3.2. Regional Forecasting Applications*

494   <u>Extreme rainfall forecasting:</u> The KSA is characterized by a hot and arid desert climate.

495   Occasionally, extreme precipitation events over the Jeddah region have led to flooding that caused

496   extensive loss of human life and damage to infrastructure (e.g. de Vries et al. 2013). The large-

497   scale features are important factors in producing regional extreme precipitation, which may exceed

498   three times the average annual rainfall. These heavy rainfall events are associated with the

499   northward extension of the Red Sea trough and intensification of the Arabian Anticyclone, which

500   provide warm moist air to the region, creating favorable conditions for the development of a short-

501   lived quasi-stationary mesoscale convective systems (Dasari et al. 2017a). Using a convective-

502   permitting WRF configuration, Viswanadhapalli et al. (2016) assessed the predictability of two

503   extreme rainfall events formed over Jeddah while assimilating various combinations of

504   conventional and satellite observations (Fig.11a). A similar WRF configuration was implemented

505   by Dasari et al. (2017b) to study the Mecca 2016 extreme rainfall event. More recently, Luong et

506   al. (2020) investigated the impact of urbanization using WRF by incorporating an urban canopy

507   model and urban land cover for several extreme weather events over Jeddah showing that

508   urbanization enhanced rainfall by ~25%.

509   <u>Oil-spill forecasting*:*</u> iReds is regularly used to support oil spill prediction efforts. As an example,

510   we have supported the Saudi authorities in the southern Red Sea by simulating a realistic oil spill

511   scenario from an abandoned oil tanker filled with oil and anchored at Ras-Isa port north of

512 Hudaydah off the coast of Yemen. The ship, which has not been operational since March 2015, is

513 corroding and there are serious concerns that the gas building up in the storage tanks could lead to

514 an explosion that might trigger an oil spill (Meredith 2019). The tanker carries an estimated volume

515 of 1 million barrels of crude oil, four times the amount of oil released in the 1989 Exxon Valdez

516 oil spill. MEDSLIK was used to model the transport and fate of oil for winter and summer

517 scenarios. Forecast winds, waves and ocean currents generated by iReds during the first two weeks

518 of February and August 2019 have been used as inputs. The oil was continuously released at the

519 tanker location (15° 15' 11" latitude and 42° 36' 52" longitude) over the two-week simulation

520 period. Fig.11b shows the concentration of oil (in barrels km^{-2}) at the end of the simulation period.

521 Following the pattern of the predicted ocean circulation, the oil was transported north-east, where

522 about 60% of its volume washed up onshore. 20% of the remaining oil formed a surface slick of

523 about 55 km^2 in size and the other 20% evaporated.

524

525 **4. Future Directions**

526 iReds has so far contributed new insights into the regional atmospheric and oceanic circulations,

527 their variability and trends in the Red Sea basin. Outputs from its various long-term simulations

528 established, in particular, a unique basin-wide eddy activity and its driving forces, a prominent

529 seasonally-varying overturning circulation modulated by the Indian monsoon, and the occasional

530 fast ventilation of its deep waters through deep water formation events forced by cold weather

531 anomalies in its northern end. The system was further critically important in supporting the

532 ongoing mega-projects along the Red Sea shores, providing unique information about the regional

533 environment to optimize the design and the operations of these new developments. It further

24

534 developed for the first time regionally-tuned forecasting capabilities that were successfully tested

535 during urgent environmental situations.

536   We are envisioning, and have already started working along several directions, to implement

537 new capabilities and continue enhancing iReds performances in the future, while further deepening

538 our understanding of the regional circulation and variability. Our ultimate goal is to develop an

539 integrated data-driven modeling and forecasting system that incorporates all available oceanic and

540 atmospheric observations in the Red Sea region and makes predictions and actionable information

541 available to scientists, government and industry, and non-expert recipients. In this regard, the first

542 Red Sea operational system is expected to be released online during 2021 to provide weekly

543 forecasts of the basin-wide atmospheric (WRF) – oceanic (MITgcm) – wave (WWIII) conditions

544 at 4km, 2km and 1km resolutions, respectively. It will be subsequently equipped with state-of-the-

545 art interactive visualization and data analytics to provide decision makers with real-time access to

546 relevant information. Future work will then focus on (i) equipping iReds with new capabilities for

547 forecasting aerosols (dust and pollution) and the marine biogeochemistry, and (ii) extending the

548 forecasting time-range of the system to subseasonal-to-seasonal and annual scales through a

549 combination of coupled modeling and data assimilation, and spatial-range to the urban and coastal

550 scales through downscaling.

551 *4.1 iReds developments*

552 Beyond the importance of predicting dust and atmospheric pollution, aerosols play a crucial role

553 in the radiation budget and the development of clouds and precipitation. They are also an important

554 source of nutrients for the Red Sea ecosystem. So far, aerosol variations have only been

555 climatologically accounted for in iReds. WRF is equipped with state-of-the-art modules to

556 simulate and study aerosols (WRF-Chem), and we have recently implemented it over the AP. We

25

557   are currently working on developing high-resolution aerosol emission inventories (natural,

558   anthropogenic, and biogenic) on daily-scales by tuning satellite remote sensing retrieval

559   algorithms with available *in situ* measurements. These will be incorporated/assimilated into WRF-

560   Chem to simulate and predict dust storms and outbreaks of industrial and urban haze pollution.

561   As part of the newly established Center of Excellence for NEOM research at KAUST, our

562   modeling system will be further expanded to investigate oceanic and atmospheric circulations at

563   the urban scales. Work is already underway with external collaborators at Imperial College (UK)

564   and Deltares Institute (Netherlands) to build the required Computational Fluid Dynamics (CFD)

565   algorithms in order to downscale our models' outputs and capabilities at these scales. In this regard,

566   we have further recently introduced and successfully tested a new dynamical downscaling

567   algorithm with WRF, based on the Continuous Data Assimilation approach (Desamsetti et al.

568   2019). Downscaling ensembles from the global operational centers remain computationally

569   demanding in terms of both computational cost and storage. We will investigate novel approaches

570   for identifying efficient downscaling of probabilistic maps through machine and dynamical

571   learning approaches.

572   In terms of data assimilation, we will continue working on enhancing the skills of our

573   ensemble system. In particular, proper accounting of model errors, for instance, through stochastic

574   perturbations and forcing ensembles greatly enhanced the assimilation results. Developing data-

575   driven approaches for quantifying the uncertainties of such perturbations and eventually estimating

576   their parameters as part of the assimilation process is our next target. To extend the time-range of

577   the system predictability, we will also strongly couple the WRF- and MITgcm-DART ensemble

578   assimilation systems to simultaneously exploit the observations of both components.

579   *5. General circulation and climate of the Red Sea and their impact on the ecosystem*

26

580   While the upper general circulation of the Red Sea is now relatively well-understood, little is still

581   known about the deep circulation. Based on chemical tracers, it has been suggested that a deep

582   overturning cell is present, but our ongoing investigations suggest a more complex 3D circulation

583   with the existence of a basin-wide cyclonic gyre in addition to the deep overturning

584   circulation. Insight into the variability and ventilation of the RSDW is needed to advance our

585   understanding of the general circulation of the Red Sea. We are further implementing non-

586   hydrostatic configurations of the MITgcm with variable-resolution curvilinear grids zooming

587   (~100m) on the straits to resolve in more detail the features of the water exchange with the Indian

588   Ocean through BaM and the water formation and sinking in the north.

589   Monitoring the decadal and seasonal variability of Red Sea ecosystem indicators, in

590   relation to the regional environmental conditions and broader climate change, is a necessity for the

591   sustainability of marine life and responsible stewardship of its socio-economical assets. Toward

592   this end, we have synergistically combined remotely-sensed ocean-color observations with our

593   models' simulations to investigate various aspects of the Red Sea ecosystem in this historically

594   data-sparse region. Remote sensing will continue to be an integral component of our system,

595   providing information for model validation and assimilation, and predicting how the ecosystem

596   indicators would respond to a changing climate. Currently, we are also developing regionally-

597   tuned algorithms for high-resolution satellite sensors (<300m resolution) that would be particularly

598   useful for tackling ecological issues in the coastal economic zone of the Red Sea. In parallel, we

599   will generate interannual simulations with the ecosystem model, which has been only investigated

600   so far with climatological physical forcing. This multidisciplinary approach is expected to offer

601   new insights into the past and current environmental status of the Red Sea coastal zone, and help

602   us to identify vulnerable regions as well as biodiversity hotspots.

27

603 *6. Coupled processes, predictability and forecasting at seasonal and climate scales*

604 The capabilities of the newly developed SKRIPS coupled model are yet to be fully exploited. We

605 will intensify studies using this system to understand coupled phenomena in the Red Sea region at

606 short- and long-term scales, and how those respond to the global climate dynamics and variations.

607 We are currently examining the outputs of the ocean-waves coupling component to investigate

608 wave-currents interactions and coastal circulations, with particular interest in the water-exchanges

609 near and over the coral reefs. Another proposed development of SKRIPS is the coupling of the

610 atmospheric chemical and marine ecosystem components to investigate regional carbon variations

611 and exchanges.

612 This coupled system will be at the core of building long-term regional predictive

613 capabilities at the subseasonal-to-seasonal through climate scales by downscaling global forecasts

614 and climate change scenarios. We will assess the system predictability of the regional phenomenon

615 at different scales, including extreme weather events (heavy rainfall, air and marine heatwaves).

616 The focus will be on identifying key factors and dynamical processes that may provide extended

617 predictability for the region and on quantifying their impact on the forecasting skills through

618 sensitivity studies. These will be then used as a guide for designing efficient, regionally-tuned,

619 data-driven strategies for projecting the weather and climate of the Red Sea and their impact on

620 the regional ecosystem and Red Sea coast.

621

622 *Acknowledgments*

625   The development of the Red Sea modeling system is being supported by the Virtual Red Sea

626   Initiative and the Competitive Research Grants (CRG) program from the Office of Sponsored

627   Research at KAUST, Saudi Aramco Company through the Saudi ARAMCO Marine

628   Environmental Center at KAUST, and by funds from KAEC, NEOM and RSP through Beacon

629   Development Company at KAUST.

630

ownloaded from http://journals.ametsoc.org/bams/article-pdf/doi/10.1175/BAMS-D-19-0005.1/5001745/bamsd190005.pdf by TEXAS A & M UNIV user on 20 October 2020

9

ccepted for publication in *Bulletin of the American Meteorological Society.* DOI 10.1175/BAMS-D-19-0005.1.

631 **List of Acronyms and Abbreviations**

3DVAR	Three-Dimensional Variational Data Assimilation
4DVAR	Four-Dimensional Variational Data Assimilation
ADCIRC	Advanced CIRCulation
AMSU	Advanced Microwave Sounding Unit
AOD	Aerosol Optical Depth
AP	Arabian Peninsula
APHRODITE	Asian Precipitation - Highly-Resolved Observational Data Integration Towards Evaluation
ASCAT	Advanced SCATterometer
AVHRR	Advanced Very-High-Resolution Radiometer
AWS	Automatic Weather Station
BaM	Bab-al-Mandeb
CCMP	Cross-Calibrated Multi-Platform
AMSU	Advanced Microwave Sounding Unit
ASCAT	Advanced SCATterometer
AVISO	Archiving, Validation and Interpretation of Satellite Oceanographic data
Chl-a	Chlorophyll-a
CFD	Computational Fluid Dynamics
CMEMS-L4	Copernicus Marine Environment Monitoring Service
CMORPH	Climate prediction center MORPHing
CMS	Connectivity Modelling System
CRU	Climatic Research Unit
DART	Data Assimilation Research Testbed
DWR	Doppler Weather Radar
EAKF	Ensemble Adjustment Kalman Filter
ECCO	Estimating the Circulation and Climate of the Ocean
ECCO2	Estimating the Circulation and Climate of the Ocean, Phase II
ECMWF	European Center for Medium-Range Weather Forecasts
EKE	Eddy Kinetic Energy
ERA	ECMWF Re-Analysis
ERSEM	European Regional Seas Ecosystem Model
ESA	European Space Agency
ESMF	Earth System Modeling Framework
FNL	Final Analysis
GAIW	Gulf of Aden Intrusion Water
GDP	Gross Domestic Product
GHRSST	Group for High Resolution Sea Surface Temperature (GHRSST)

GLORYS2	GLobal Ocean ReanalYSis 2
GPSRO	Global Position System Radio Occultation
HYCOM	HYbrid Coordinate Ocean Model
HYSPLIT	Hybrid Single-Particle Lagrangian Integrated Trajectory
iReds-M1	integrated data-driven Red Sea Modeling system version 1
KAEC	King Abdullah Economic City
KAUST	King Abdullah University of Science and Technology
KSA	Kingdom of Saudi Arabia
LME	Large Marine Ecosystem
MITgcm	Massachusetts Institute of Technology general circulation model
NCEP	National Centers for Environmental Prediction
NUOPC	National United Operational Prediction Capability
OC-CCI	Ocean Colour Climate Change Initiative
OLCI	Ocean and Land Color Instrument
OSTIA	Operational Sea Surface Temperature and Sea Ice Analysis
OTIS	Ohio state university Tidal Inversion Software
PME	Presidency of Meteorology and Environment
RADS	Radar Altimeter Database
RMSE	Root-Mean-Square-Error
RSDW	Red Sea Deep Water
RSOW	Red Sea Outflow Water
RSP	Red Sea Project
SKRIPS	Scripps-KAUST Regional Integrated Prediction System
SSH	Sea Surface Height
SST	Sea Surface Temperature
SWAN	Simulating WAves Nearshore
TRMM	Tropical Rainfall Measuring Mission
WHOI	Woods Hole Oceanographic Institution
WOA	World Ocean Atlas
WRF	Weather Research and Forecasting
WWIII	WaveWatch-III

632

31

References

633   **References**

634   Afzal, S., M. Hittawe, S. Ghani, T. Jamil, O. Knio, M. Hadwiger, and I. Hoteit, 2019a: The state

635   of the art in visual analysis approaches for ocean and atmospheric datasets. Computer

636   Graphics Forum, 38: 881-907.

637   Afzal, S., S. Ghani, G. Tissington, S. Langodan, H. P. Dasari, D. Raitsos, J. Gittings, T. Jamil, M.

638   Srinivasan, and I. Hoteit, 2019b: RedSeaAtlas: A visual analytics tool for spatio-temporal

639   multivariate data of the Red Sea. Workshop on Visualization in Environmental Sciences

640   (EnvirVis), doi:10.2312/envirvis.20191101.

641   Albarakati, S., R. M. Lima, L. Giraldi, I. Hoteit, and O. Knio, 2019: Optimal 3D trajectory planning

642   for AUVs using ocean general circulation models. Ocean Engineering, 188, 106266.

643   Anderson, J., T. Hoar, K. Raeder, H. Liu, N. Collins, R. Torn, and A. Avellano, 2009: The Data

644   Assimilation Research Testbed: A community dacility. Bull. Amer. Meteor. Soc., 90, 1283-

645   1296.

646   Antony, C., S. Langodan, P. R. Shanas, H. P. Dasari, Y. Abualnaja, O. Knio, and I. Hoteit, 2019:

647   Modelling extreme water levels along the central Red Sea coast of Saudi Arabia-Processes

648   and frequency analysis. Natural Hazards, under review.

649   Ardhuin, F., E. Rogers, V. Babanin, J. F. Filipot, A. Roland, A. Van der Westhuysen, P.

650   Queffeoulou, J. M. Lefevre, A. Lotfi, and F. Collard, 2010: Semiempirical dissipation

651   source functions for ocean waves. Part I: Definition, calibration and validation. J. Phys.

652   Oceanogr., 40, 1917-1941.

32

653 Attada, R., H. P. Dasari, J. S. Chowdary, Y. Ramesh Kumar, O. Knio, and I. Hoteit, 2018a: Surface

654   air temperature variability over the Arabian Peninsula and its links to circulation patterns.

655   Int. J. Climatol., 39(1), 445-464.

656 Attada R., H. P. Dasari, A. Parekh, J. S. Chowdary, S. Langodan, O. Knio, and I. Hoteit, 2018b:

657   The role of the Indian Summer Monsoon variability on Arabian Peninsula summer climate.

658   Clim. Dyn., 52, 3389.

659 Attada, R., K. Ravi Kumar, Y. Ramesh Kumar, H. P. Dasari, O. Knio, and I. Hoteit, 2018c:

660   Prominent modes of summer surface air temperature variability and associated circulation

661   anomalies   over   the   Arabian   Peninsula.   Atmos.   Sci.   Lett.,   19:e860,

662   https://doi.org/10.1002/asl.860.

663 Baretta, J. W., W. Ebenhoh, and P. Ruardij, 1995: The European-Regional-Seas-Ecosystem-

664   Model, a complex marine ecosystem model. Neth. J. Sea Res., 33, 233-246.

665 Barker, D., X.-Y. Huang, Z. Liu, T. Auligné, X. Zhang, S. Rugg, R. Ajjaji, A. Bourgeois, J. Bray,

666   Y. Chen, M. Demirtas, Y.-R. Guo, T. Henderson, W. Huang, H.-C. Lin, J. Michalakes, S.

667   Rizvi, and X. Zhang, 2012: The Weather Research and Forecasting Model's Community

668   Variational/Ensemble Data Assimilation System: WRFDA. Bull. Amer. Meteor. Soc., 93,

669   831–843.

670 Belkin, I. M., 2009: Rapid warming of Large Marine Ecosystems. Prog. Oceanogr., 81, 207–213.

671 Booij, N., R. C. Ris, and L. H. Holthuijsen, 1999: A third-generation wave model for coastal

672   regions. Part 1: Model description and validation. J. Geophys. Res., 104, 7649-7666.

673   Bower, A. S., and J. T. Farrar, 2015: Air–Sea Interaction and Horizontal Circulation in the Red

674   Sea. N.M.A. Rasul and I.C.F. Stewart, Eds., Vol. 1900 of Springer Earth System Sciences,

675   Springer Berlin Heidelberg, 329-342.

676   Brewin B., X. A. G. Morán, D. E. Raitsos, J. Gittings, M. L. Calleja, M. S. Viegas, M. I. Ansari,

677   N. Al-Otaibi, T. M. Huete-Stauffer, and I. Hoteit, 2019: Factors regulating the relationship

678   between total and size-fractionated chlorophyll-a in coastal waters of the Red Sea. Frontiers

679   in Microbiology, 10, 1964.

680   Brewin, R. J. W., D. E. Raitsos, G. Dall'Olmo, N. Zarokanellos, T. Jackson, M-F. Racault, E. S.

681   Boss, S. Sathyendranath, B. H. Jones, and I. Hoteit, 2015: Regional ocean-colour

682   chlorophyll algorithms for the Red Sea. Remote Sensing of Environment, 162, 257-270.

683   Brewin, R. J. W., D. E. Raitsos, Y. Pradhan, and I. Hoteit, 2013: Comparison of chlorophyll in the

684   Red Sea derived from MODIS-Aqua and in vivo fluorescence. Remote Sensing of

685   Environment, 136, 218-224.

686   Cantin, N. E., A. L. Cohen, K. B. Karnauskas, A. M. Tarrant, and D. C. McCorkle, 2010: Ocean

687   warming slows coral growth in the central Red Sea. Science, 329, 322-325.

688   Carvalho, S., B. Kürten, G. Krokos, I. Hoteit, and J. Ellis, 2018: The Red Sea. Book Chapter in

689   World Seas: An Environmental Evaluation – vol.II: the Indian Ocean to the Pacific, Chapter

690   3, 49-74.

691   Cember, R. P. 1988: On the sources, formation, and circulation of Red Sea deep water. J. Geophys.

692   Res., 93, 8175-8191.

693   Chaidez, V., D. Dreano, S. Agusti, C. M. Duarte, and I. Hoteit, 2017: Decadal trends in Red Sea

694   maximum surface temperature. Sci. Rep., 7, 8144.

695   Churchill, J. H., Y. Abualnaja, R. Limeburner, and M. Nellayaputhenpeedika, 2018: The dynamics

696   of weather-band sea level variations in the Red Sea. Regional Studies in Marine Science, 24,

697   336-342.

698   Collingridge, K., 2012: Modelling risk areas in the North Sea for blooms of the invasive comb

699   jellyfish Mnemiopsis Leidyi. CEFAS Summer Proj., 9, 21-36.

700   da Silva, J., J. Magalhaes, T. Gerkema, and L. Maas, 2012: Internal solitary waves in the Red Sea:

701   An unfolding mystery. Oceanography, 25, 96-107.

702   Dasari, H. P., L. Sabique, V. Yesubabu, V. B. Rao, V. P. Papadopoulos, and I. Hoteit, 2017a:

703   ENSO influence on the Red Sea Convergence Zone and Associated Rainfall. Int. J.

704   Climatol., doi:10.1002/joc.5208.

705   Dasari, H. P., A. Raju, O. Knio, and I. Hoteit, 2017b: Analysis of a severe weather event over

706   Mecca, Kingdom of Saudi Arabia using observations and high-resolution modeling.

707   Meteorological Applications, doi:10.1002/met.1662.

708   Dasari, H. P., S. Desamsetti, S. Langodan, R. Attada, R. K. Kunchala, Y. Viswanadhapalli, O.

709   Knio, and I. Hoteit, 2019a: High-resolution assessment of solar energy resources over the

710   Arabian Peninsula. Applied Energy, 248, 354-371.

711   Dasari, H. P., D. Srinivas, S. Langodan, R. Attada, A. Karumuri, and I. Hoteit, 2019b:

712   Multidecadal variability of the Arabian Peninsula rainfall and its relationship with the

713   ENSO signals in the tropical Indo-Pacific. J. Climate, under revision.

714   Dasari, H. P., S. Desamsetti, S. Langodan, S. Singh, L. N. K. Ramakrishna, and I. Hoteit, 2020:

715   Air-quality assessment over NEOM, Kingdom of Saudi Arabia. Atmospheric Environment,

716   230, doi:10.1016/j.atmosenv.2020.117489.

717

718   Davis, S. R., L. J. Pratt and H. Jiang, 2015: The Tokar Gap: Regional circulation, diurnal

719   variability, and moisture transport based on numerical simulations. J. Climate, 28, 5585-

720   5907.

721   De Dominicis, M., N. Pinardi, G. Zodiatis, and R. Lardner, 2013b: MEDSLIK-II, a Lagrangian

722   marine surface oil spill model for short-term forecasting - Part I: Theory. Geosci. Model.

723   Dev., 6, 1851-1869.

724   De Dominicis, M., N. Pinardi, G. Zodiatis, and R. Archetti, 2013a: MEDSLIK-II, a Lagrangian

725   marine surface oil spill model for short-term forecasting - Part II: Numerical simulations

726   and validations. Geosci. Model. Dev., 6, 1871-1888.

727   de Vries, A. J., E. Tyrlis, D. Edry, S. O. Krichak, B. Steil, and J. Lelieveld, 2013: Extreme

728   precipitation events in the Middle East: Dynamics of the Active Red Sea Trough. J.

729   Geophys. Res., 118, 7087-7108.

730   Deltares, 2016: Delft3D-FLOW. Simulation of multi-dimensional hydrodynamic flow and

731   transport phenomena, including sediments – User Manual, Version 3.15, Deltares, Delft,

732   The Netherlands.

733   Desamsetti, S., H. P. Dasari, S. Langodan, E. S. Titi, O. Knio, and I. Hoteit, 2019: Efficient

734   dynamical downscaling of general circulation models Using continuous data assimilation.

735   Q. J. Roy. Meteor. Soc., 245, 3175-3194.

736   Draxler, R. R., and G. D. Hess, 1997: Description of the HYSPLIT_4 modeling system. NOAA

737   Tech. Memo. ERL ARL-224, NOAA/Air Resources Laboratory, Silver Spring, MD, 24 pp.

36

738   Dreano, D., D. E. Raitsos, J. Gittings, G. Krokos, and I. Hoteit, 2016: The Gulf of Aden

739   intermediate water intrusion regulates the Southern Red Sea summer phytoplankton blooms.

740   PLoS One, 11(12), e0168440.

741   Edwards, A., and S. Head, 1986: Red Sea key environment. Headington Hill Hall, Oxford, UK:

742   Pergamon Press.

743   Edwards, C., A. Moore, I. Hoteit, and B. Cornuelle, 2015: Regional ocean data assimilation.

744   Annual Review of Marine Science, 7, 21-42.

745   Ellis, J.I., T. Jamil, H. Anlauf, D.J. Coker, J. Curdia, J. Hewitt, B.H. Jones, G. Krokos, B. Kurten,

746   H.D. Prasad, F. Rooth, S. Carvalho, and I. Hoteit, 2019: Multiple stressor effects on coral

747   reef ecosystems. Global Change Biology, 25(12), 4131-4146.

748   El Mohtar, S., I. Hoteit, O. Knio, L. Issa, and I. Lakkis, 2018: Lagrangian tracking in stochastic

749   fields with application to an ensemble of velocity fields in the Red Sea. Ocean Modelling,

750   131, 1-14.

751   Eshel, G., M. A. Cane, and M. B. Blumenthal, 1994: Modes of subsurface, intermediate, and deep

752   water renewal in the Red Sea. J. Geophys. Res., 99, 15941-15952.

753   Genevier, L. G. C., T. Jamil, D. E. Raitsos, G. Krokos, and I. Hoteit, 2019: Marine heatwaves

754   reveal coral reef zones susceptible to bleaching in the Red Sea. Global Change Biol, 25,

755   2338-2351.

756   Gimeno, L., A. Drumond, R. Nieto, R. M. Trigo, and A. Stohl, 2010: On the origin of continental

757   precipitation. Geophys. Res. Let., 37(13), doi:10.1029/2010GL043712.

758   Gittings, J. A., D. E. Raitsos, G. Krokos, and I. Hoteit, 2018: Impacts of warming on phytoplankton

759   abundance and phenology in a typical tropical marine ecosystem. Sci. Rep., 8, 2240.

37

760   Gittings J. A., R. J. W. Brewin, D. E. Raitsos, M. Kheireddine, M. Ouhssain, B. H. Johns, and I.

761   Hoteit, 2019a: Remotely sensing phytoplankton size structure in the Red Sea. Remote

762   Sensing of Environment, 234, 111387.

763   Gittings, J. A., D. E. Raitsos, M. Kheireddine, M. F. Racault, H. Claustre, and I. Hoteit, 2019b:

764   Evaluating tropical phytoplankton phenology metrics using contemporary tools. Sci. Rep.,

765   9, 674.

766   Guo, D. Q., T. R. Akylas, P. Zhan, A. Kartadikaria, and I. Hoteit, 2016: On the generation and

767   evolution of internal solitary waves in the southern Red Sea. J. Geophys. Res., 121, 8566-

768   8584.

769   Guo, D. Q., A. Kartadikaria, P. Zhan, J. S. Xie, M. J. Li, and I. Hoteit, 2018: Baroclinic tides

770   simulation in the Red Sea: comparison to observations and basic characteristics. J. Geophys.

771   Res., 123, 9389-9404.

772   Guo, D., P. Zhan, and I. Hoteit 2020: Numerical study of shoaling process of internal solitary

773   waves in the southern Red Sea. Journal of Geophysical Research, under revision.

774   Hadri, B., S. Kortas, S. Feki, R. Khurram, and G. Newby, 2015: Overview of the KAUST's Cray

775   X40 system–Shaheen II. Proceedings of the 2015 Cray User Group.

776   Hill, C., C. DeLuca, Balaji, M. Suarez, and A. Silva, 2004: The architecture of the earth system

777   modeling framework. Comp. Sci. Eng., 6, 18-28.

778   Höllt, T., A. Magdy, G. Chen, G. Gopalakrishnan, I. Hoteit, C. D. Hansen, and M. Hadwiger,

779   2013: Visual Analysis of uncertainties in ocean forecasts for planning and operation of off-

780   Shore structures. IEEE Pacific Visualization Symposium, pp. 59-66.

781   Höllt, T., A. Magdy, P. Zhan, G. Chen, G. Gopalakrishnan, I. Hoteit, C.D. Hansen, and M.

782   Hadwiger, 2014: Ovis: A Framework for Visual Analysis of Ocean Forecast Ensembles.

783   IEEE Transactions on Visualization and Computer Graphics, 20, 1114-1126.

784   Höllt, T., M. Hadwiger, O. Knio, and I. Hoteit, 2015: Probability maps for the visualization of

785   assimilation ensemble flow data. Workshop on Visualization in Environmental Sciences

786   (EnvirVis), pp.43-47.

787   Hoteit, I., B. Cornuelle, A. Köhl, and D. Stammer: Treating strong adjoint sensitivities in tropical

788   eddy-permitting variational data assimilation, 2006: Q. J. Roy. Meteor. Soc., 131, 3659-

789   3682.

790   Hoteit, I., T. Hoar, G. Gopalakrishnan, J. Anderson, N. Collins, B. Cornuelle, A. Kohl, and P.

791   Heimbach, 2013: A MITgcm/DART ocean prediction and analysis system with application

792   to the Gulf of Mexico. Dynamics of Atmospheres and Oceans, 63, 1-23.

793   Hoteit, I., D. T. Pham, M. E. Gharamti and X. Luo, 2015: Mitigating observation perturbation

794   sampling errors in the stochastic EnKF. Mon. Wea. Rev., 143, 2918-2936.

795   Hoteit, I., X. Luo, M. Bocquet, A. Kohl, and B. Ait-El-Fquih, 2018: Data Assimilation in

796   Oceanography: Current Status and New Directions. Book Chapter, New Frontiers in

797   Operational Oceanography, Editors: E. P. Chassignet, A. Pascual, J. Tintore, and J. Verron,

798   GODAE Ocean View, 815pp, https://doi.org/10.17125/gov2018.

799   Ioc, I., 2003: BODC 2003 - Centenary Edition of the GEBCO Digital Atlas, published on CD-

800   ROM on behalf of the Intergovernmental Oceanographic Commission and the International

801   Hydrographic Organization as part of the General Bathymetric Chart of the Oceans, British

802   oceanographic data centre, Liverpool.

39

803   Krokos, G., V. P. Papadopoulos, S. S. Sofianos, H. Ombao, P. Dybczak, and I. Hoteit, 2019:

804   Natural climate oscillations may counteract Red Sea warming over the coming decades.

805   Geophys. Res. Lett., 46, 3454-3461.

806   G. Krokos, I. Cerovecki, P. Zhan, M. C. Hendershott, I. Hoteit (2020). Seasonal Evolution of

807   Mixed Layers in the Red Sea and the Relative Contribution of Atmospheric Buoyancy and

808   Momentum Forcing. Journal of Geophysical Research, under review, 2020

809   Kunchala, R., R. Attada, H. P. Dasari, V. R. Kumar, S. Langodan, Y. Abualnaja, and I. Hoteit,

810   2018: Aerosol optical depth variability over the Arabian Peninsula using satellite and

811   ground based observations. Atmospheric Environment, 187, 346-357.

812   Kunchala, R. K., R. Attada, H. P. Dasari, K. Ramesh, Y. Abualnaja, K. Ashok, and I. Hoteit, 2019:

813   On the recent amplification of dust over the Arabian Peninsula during 2002-2012. J.

814   Geophys. Res., doi: 10.1029/2019JD030695.

815   Langodan, S., L. Cavaleri, Y. Viswanadhapalli, and I. Hoteit, 2014: The Red Sea: a natural

816   laboratory for wind and wave modeling. J. Phys. Oceanogr. 44, 3139-3159.

817   Langodan, S., L. Cavaleri, Y. Viswanadhapalli, and I. Hoteit, 2015: Wind-wave source functions

818   in opposing seas. J. Geoph. Res., 120, 6751-6768.

819   Langodan, S., Y. Viswanadhapalli, H. P. Dasari, O. Knio, and I. Hoteit, 2016a: A high

820   resolution assessment of wind and wave energy potentials in the Red Sea. Applied

821   Energy, 181, 244-255.

822   Langodan, S., V. Yesubabu, and I. Hoteit, 2016b: Impact of atmospheric data assimilation on

823   waves in the Red Sea. Ocean Engineering, 116, 200-215.

824   Langodan, S., L. Cavaleri, A. Pomaro, V. Yesubabu, L. Bertotti, and I. Hoteit, 2017a: The

825   climatology of the Red Sea – Part 1: The winds. Int. J. Climatol., 37, 4518-4528.

826   Langodan, S., L. Cavaleri, A. Pomaro, V. Yesubabu, L. Bertotti, and I. Hoteit, 2017b: The

827   climatology of the Red Sea – Part 2: The waves. Int. J. Climatol., 37, 4518-4528.

828   Langodan, S., L. Cavaleri, A. Pomaro, J. Portilla, Y. Abualnaja, and I. Hoteit, 2018: Unraveling

829   climatic wind and wave trends in the Red Sea using wave spectra partitioning. J. Climate,

830   31, 1881-1895.

831   Langodan, S., L. Cavaleri, J. Portilla, Y. Abualnaja, and I. Hoteit, 2020a: Can we extrapolate

832   climate in an inner basin? The case of the Red Sea. Global and Planetary Change, 188,

833   103151.

834   Langodan, S., C. Antony, P.R. Shanas, H. P. Dasari, Y. Abualnaja, O. Knio, and I. Hoteit,

835   2020b: Wave modeling of a reef-sheltered coastal zone in the Red Sea. Ocean Engineering,

836   207, 107378.

837   Luettich, R.A., and J. J. Westerink, 2004: Formulation and numerical implementation of the 2D/3D

838   ADCIRC finite element model Version 44.XX. ADCIRC Tech. Rep., 74 pp.

839   Luong, T. M., H. P. Dasari, and I. Hoteit, 2019: Impact of urbanization on the simulation of

840   extreme rainfall in Jeddah, Saudi Arabia. Journal of Applied Meteorology and Climatology,

841   5, 952-971.

842   Marshall, J., A. Adcroft, C. Hill, L. Perelman, and C. Heisey, 1997a: A finite-volume,

843   incompressible Navier Stokes model for studies of the ocean on parallel computers. J.

844   Geophys. Res., 102, 5753-5766.

845   Marshall, J., C. Hill, L. Perelman, and A. Adcroft, 1997b: Hydrostatic, quasi-hydrostatic, and

846   nonhydrostatic ocean modeling. J. Geophys. Res., 102, 5733-5752.

847   Meredith, S., 2019: 'Floating bomb': Decaying oil tanker near Yemen coast could soon explode,

848   experts warn. CNBC, 24 July 2019, https://www.cnbc.com/2019/07/24/oil-tanker-near-

849   yemen-coast-could-soon-explode-experts-warn.html, accessed on 12 December 2019.

850   Nanninga, G. B., P. Saenz-Agudelo, P. Zhan, I. Hoteit, and M. L. Berumen, 2015: Not finding

851   Nemo: limited reef-scale retention in a coral reef fish. Coral Reefs, 34, 383-392.

852   Osman, E. O., D. J. Smith, M. Ziegler, B. Kürten, C. Conrad, K. M. El- Haddad, C.R. Voolstra,

853   and D. J. Suggett, 2018: Thermal refugia against coral bleaching throughout the northern

854   Red Sea. Global Change Biology, 24, 474-484.

855   Papadopoulos, V. P., Y. Abualnaja, S. A. Josey, A. S. Bower, D. E. Raitsos, H. Kontoyiannis, and

856   I. Hoteit, 2013: Atmospheric forcing of the winter air–sea heat fluxes over the northern Red

857   Sea. J. Clim., 26, 1685-1701.

858   Papadopoulos, V.P., P. Zhan, S.S. Sofianos, D.E. Raitsos, M. Qurban, Y. Abualnaja, A. Bower,

859   H. Kontoyiannis, A. Pavlidou, T. T. Mohamed Asharaf, N. Zarokanellos, and I. Hoteit,

860   2015: Factors governing the deep ventilation of the Red Sea. J. Geophys. Res., Oceans, 120,

861   7493-7505.

862   Paris, C. B., J. Helgers, E. van Sebille, and A. Srinivasan, 2013: Connectivity Modeling System:

863   A probabilistic modeling tool for the multi-scale tracking of biotic and abiotic variability in

864   the ocean. Environ. Modell. Softw., 42, 47-54.

865   Patzert, W. C., 1974: Wind induced reversal in the Red Sea circulation. Deep-Sea Res., 21, 109-

866   121.

42

867   Petihakis, G., G. Triantafyllou, I. J. Allen, I. Hoteit, and C. Dounas, 2002: Modelling the spatial

868   and temporal variability of the Cretan Sea ecosystem. J. Mar. Sys., 36, 173-196.

869   Pratt, L. J., H. E. Deese, S. P. Murray and W. Johns, 2000: Continuous dynamical nodes in straits

870   having arbitrary cross sections, with applications to the Bab-al-Mandab. J. Phys. Oceanogr.,

871   30, 2515-2534.

872   Raboudi, N. F., B. Ait-El-Fquih, and I. Hoteit, 2018: Ensemble Kalman filtering with one-step-

873   ahead smoothing. Mon. Wea. Rev., 146, 561-581.

874   Racault, M.-F., D. E. Raitsos, M. L. Berumen, R. J. W. Brewin, T. Platt, S. Sathyendranath, and I.

875   Hoteit, 2015: Phytoplankton phenology indices in coral reef ecosystems: Application to

876   ocean-color observations in the Red Sea. Remote Sensing of Environment, 160, 222-234.

877   Raitsos, D. E., I. Hoteit, P. K. Prihartato, T. Chronis, G. Triantafyllou, and Y. Abualnaja, 2011:

878   Abrupt warming of the Red Sea. Geophys. Res. Lett., 38, doi:10.1029/2011GL047984.

879   Raitsos, D. E., Y. Pradhan, R. J. W. Brewin, G. Stenchikov, and I. Hoteit, 2013: Remote sensing

880   the phytoplankton seasonal succession of the Red Sea. PLoS One, 8, e64909,

881   doi:10.1371/journal.pone.0064909.

882   Raitsos, D. E., X. Yi, T. Platt, M.-F. Racault, R.J.W. Brewin, Y. Pradhan, V.P. Papadopoulos, S.

883   Sathyendranath, and I. Hoteit, 2015: Monsoon oscillations regulate fertility of the Red Sea.

884   Geophys. Res. Lett., 42, 855-862.

885   Raitsos, D. E., R. J. W. Brewin, P. Zhan, D. Dreano, Y. Pradhan, G. B. Nanninga, and I. Hoteit,

886   2017: Sensing coral reef connectivity pathways from space. Sci. Rep., 7, 9338.

887   Ralston, D. K., H. Jiang, and T. F. Ferrar, 2013: Waves in Red Sea: Response to monsoonal and

888   mountain gap winds. Continental Shelf Research, 65, 1-13.

43

889 Sathyendranath, S., R.J.W. Brewin, C. Brockmann, V. Brotas, B. Calton, A. Chuprin, P. Cipollini,

890   A.B. Couto, J. Dingle, R. Doerffer, C. Donlon, M. Dowell, A. Farman, M. Grant, A. Groom,

891   A. Horseman, T. Jackson, H. Krasemann, S. Lavender, V. Martinez-Vicente, C. Mazeran,

892   F. Mélin, T.S. Moore, D. Müller, P. Regner, S. Roy, C.J. Steele, F. Steinmetz, J. Swinton,

893   M. Taberner, A. Thompson, A. Valente, M. Zühlke, V.E. Brando, H. Feng, G. Feldman,

894   B.A. Franz, R. Frouin, R.W. Gould, S.B. Hooker, M. Kahru, S. Kratzer, B.G. Mitchell, F.

895   Muller-Karger, H.M. Sosik, K.J. Voss, J. Werdell, amd T. Platt, 2019: An ocean-colour time

896   series for use in climate studies: the experience of the Ocean-Colour Climate Change

897   Initiative (OC-CCI). Sensors, 19, 4285.

898 Sivareddy, S., H. Toye, P. Zhan, S. Langodan, G. Krokos, O. Knio, and I. Hoteit, 2019: Impact of

899   Atmospheric and Model Physics Perturbations on a High-Resolution Ensemble Data

900   Assimilation System of the Red Sea. Journal of Geophysical research, under review.

901 Skamarock, W. C., J. B. Klemp, J. Dudhia, D. O. Gill, Z. Liu, J. Berner, W. Wang, J. G. Powers,

902   M. G. Duda, D. M. Barker, and X.-Y. Huang, 2019: A Description of the Advanced

903   Research WRF Version 4. NCAR Tech. Note NCAR/TN-556+STR, 145 pp.

904   doi:10.5065/1dfh-6p97.

905 Smeed, D., 1997: Seasonal variation of the flow in the strait of Bab-al-Mandab. Oceanol. Acta,

906   20, 773-781.

907 Sofianos, S., and W. E. Johns, 2007: Observations of the summer Red Sea circulation. J. Geophys.

908   Res., 112, 1-20.

909 Sofianos, S., and W. E. Johns, 2015: The Red Sea: Water mass formation, Overturning Circulation,

910   and the Exchange of the Red Sea with the Adjacent Basins. (N. M. A. Rasul & I. C. F.

911   Stewart, Eds.). Berlin, Heidelberg: Springer Berlin Heidelberg.

44

912   Stammer, D., C. Wunsch, R. Giering, C. Eckert, P. Heimbach, J. Marotzke, A. Adcroft, C. N. Hill,

913   and J. Marshall, 2002: The global ocean circulation during 1992–1997, estimated from

914   ocean observations and a general circulation model. J. Geophys. Res., 107, 3118.

915   Sun, R., A. C. Subramanian, A. J. Miller, M. R. Mazloff, I. Hoteit, and B. D. Cornuelle, 2019:

916   SKRIPS v1. 0: a regional coupled ocean-atmosphere modeling framework (MITgcm-WRF)

917   using ESMF/NUOPC, description and preliminary results for the Red Sea. Geosci. Model.

918   Dev., 12, 4221-4244.

919   Tolman, H. L., 2008: User manual and system documentation of WAVEWATCH-III version 3.14.

920   Technical Note Nr.268, pp.25-32, NOAA/NWS/NCEP/OMB.

921   Toye, H., P. Zhan, G. Gopalakrishnan, A. R. Kartadikaria, H. Huang, O. Knio, and I. Hoteit, 2017:

922   Ensemble data assimilation in the Red Sea: sensitivity to ensemble selection and

923   atmospheric forcing. Ocean Dynamics, 67, 915-933.

924   Toye, H., S. Kortas, P. Zhan, and I. Hoteit, 2018: A fault-tolerant HPC scheduler extension for

925   large and operational ensemble data assimilation: Application to the Red Sea. J. Comp. Sci.,

926   27, 46-56.

927   Toye, H., S. Sivareddy, N. Raboudi, and I. Hoteit, 2019: A Hybrid ensemble data assimilation

928   system for the Red Sea: Implementation and Evaluation. Q. J. R. Meteo. Soc., under review.

929   Triantafyllou, G., F. Yao, G. Petihakis, K. Tsiaras, D. E. Raitsos, and I. Hoteit, 2014: Exploring

930   the Red Sea seasonal ecosystem functioning using a three-dimensional biophysical model.

931   J. Geophys. Res., 119, 1791-1811.

932   Viswanadhapalli, Y., C. V. Srinivas, S. Langodan, and I. Hoteit, 2016: Predicting extreme rainfall

933   events over Jeddah, Saudi Arabia: impact of data assimilation with conventional and

934   satellite observations. Q. J. Roy. Meteor. Soc., 142, 327-348.

935   Viswanadhapalli, Y., H. P. Dasari, S. Langodan, V. S. Challa, and I. Hoteit, 2017: Climatic

936   features of the Red Sea from a regional assimilative model. Int. J. Climatol., 37, 2563-2581.

937   Viswanadhapalli, Y., H. P. Dasari, S. Dwivedi, V. R. Madineni, S. Langodan, and I. Hoteit, 2019:

938   Variability of monsoon low- level jet and associated rainfall over India. Int. J. Climatol.,

939   doi:10.1002/joc.6256.

940   Wang, T., Le Maître, I. Hoteit, and O. Knio, 2016: Path planning in uncertain flow fields using

941   ensemble method. Ocean Dynamics, 66, 1231-1251.

942   Wang, Y., D. E. Raitsos, G. Krokos, J. A. Gittings, P. Zhan, and I. Hoteit, 2019: Physical

943   connectivity simulations reveal dynamic linkages between coral reefs in the southern Red

944   Sea and the Indian Ocean. Sci. Rep., 9, 16598.

945   Xie, J. S., G. Krokos, S. Sofianos, and I. Hoteit, 2019: Interannual Variability of the Exchange

946   Flow Through the Strait of Bab-al-Mandeb. J. Geophys. Res., 124, 1988-2009.

947   Yao, F. C., I. Hoteit, L. J. Pratt, A. S. Bower, A. Köhl, G. Gopalakrishnan, and D. Rivas, 2014a:

948   Seasonal overturning circulation in the Red Sea. Part-II: Winter circulation. J. Geophys.

949   Res., 119, 2263-2289.

950   Yao, F. C., I. Hoteit, L. J. Pratt, A. S. Bower, P. Zhai, A. Köhl, and G. Gopalakrishnan, 2014b:

951   Seasonal overturning circulation in the Red Sea. Part-I: Model validation and summer

952   circulation. J. Geophys. Res., 119, 2238-2262.

953   Yao, F., and I. Hoteit, 2018: Rapid red sea deep water renewals caused by volcanic eruptions and

954   the north Atlantic oscillation. Science advances, 4(6), eaar5637.

955   Zhai, P., and A. S. Bower, 2013: The response of the Red Sea to a strong wind jet near the Tokar

956   Gap in summer. J. Geophys. Res. Oceans, 118, 422-434.

957   Zhai, P., A.S. Bower, W.M. Smlethie Jr., and L.J. Pratt, 2015: Formation and spreading of Red

958   Sea Outflow Water in the Red Sea, J. Geophys. Res., Oceans, 120, 6542-6563.

959   Zhan, P., A. C. Subramanian, F. C. Yao, and I. Hoteit, 2014: Eddies in the Red Sea: A statistical

960   and dynamical study. J. Geophys. Res., 119, 3909-3925.

961   Zhan, P., F. Yao, A. R. Kartadikaria, Y. Viswanadhapalli, G. Gopalakrishnan, and I. Hoteit, 2015:

962   Far-Field ocean conditions and concentrate discharges modeling along the Saudi coast of

963   the Red Sea. Environ. Sci. Eng., 501-520, doi:10.1007/978-3-319-13203-7-21.

964   Zhan, P., A. C. Subramanian, F. C. Yao, A. R. Kartadikaria, D. Q. Guo, and I. Hoteit, 2016: The

965   eddy kinetic energy budget in the Red Sea. J. Geophys. Res., 121, 4732-4747.

966   Zhan, P., G. Gopalakrishnan, A. C. Subramanian, D. Guo, and I. Hoteit, 2018: Sensitivity Studies

967   of the Red Sea Eddies Using Adjoint Method. J. Geophys. Res., 123, 8329-8345.

968   Zhan, P., G. Krokos, D. Guo, and I. Hoteit, 2019: Three-Dimensional Signature of the Red Sea

969   Eddies and Eddy-Induced Transport. Geophys. Res. Lett., 46, 2167-2177.

970   Zodiatis, G., R. Lardner, T. M. Alves, Y. Krestenitis, L. Perivoliotis, S. Sofianos and K.

971   Spanoudaki, 2019: Oil spill forecasting (prediction) in: THE SEA. The Science of Ocean

972   Prediction, Yale University, Number 17, 923-953.

973

974

975   Table 1. A variety of *in situ* and satellite observations, and reanalysis datasets are being used to

976   study the regional ocean and atmospheric variabilities and changes, to validate our models,

977   for prescribing model boundary conditions, and for initialization and assimilation. We have

978   also developed regionally-tuned remote sensing algorithms, based on local observations,

979   to generate improved Chlorophyll datasets for the Red Sea region (Brewin et al., 2019).

980   Details of the datasets, and their use, are listed in the Table below.

Datasets and observations	Type	Usage
Atmospheric Datasets		
ERA-Interim, NCEP FNL, Real-time Global SST, CCMP, CRU	Reanalyses	Initialization and Boundaries
AMSU, QuikSCAT, ASCAT, GPSRO	Satellite	
TRMM, CMORPH, APHRODITE	Rainfall reanalysis	Model validation
Rain gauge precipitation, AWS-PME, KSA Saudi Aramco, KSA RADAR, PME, KSA KAUST-WHOI BUOY Synoptic and Upper - Uni. of Wyoming	Local Met-Ocean	Assimilation and validation
Globwave altimeter wave data	Significant wave height	Wave model validation
Oceanic Datasets		
ECCO2, WOA, GLORYS2	Reanalyses	Initialization and Boundaries
AVHRR, RADS	Satellite	Assimilation and validation
RSP, NEOM, Saudi Aramco Tidal Gauges, KAUST-WHOI BUOY	In-situ Observations	Model validation
OSTIA, AVISO	Satellite	
OTIS	Simulation	Tidal forcing
ESA: Ocean Colour Climate Change Initiative – OC-CCI and Sentinel-3 OLCI	Satellite	Ocean colour / Ecological Indicators

981

982

48

Figures

984

985
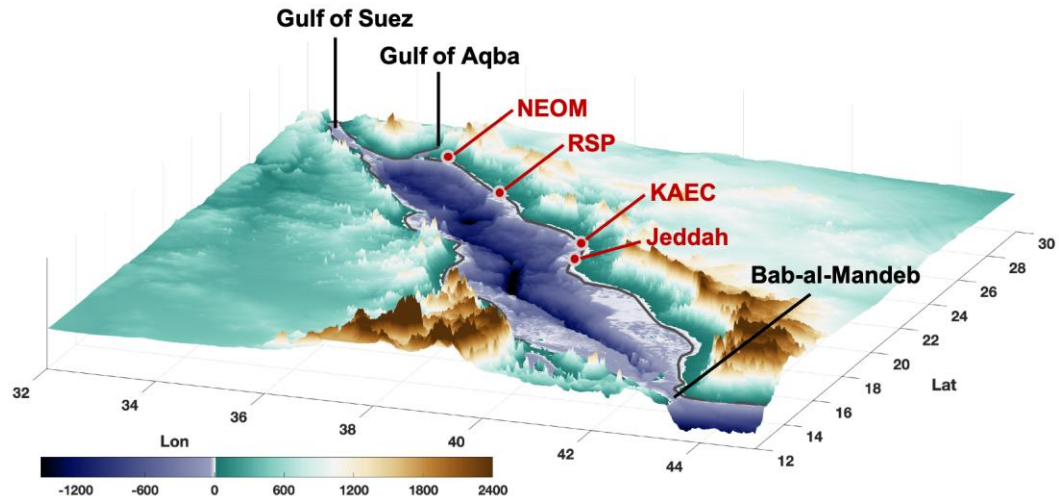
986

987   Figure 1. Topography of the Red Sea region. The important sites along the Saudi coastline are

988   indicated on the map.

989

990

49

991

992

993

994
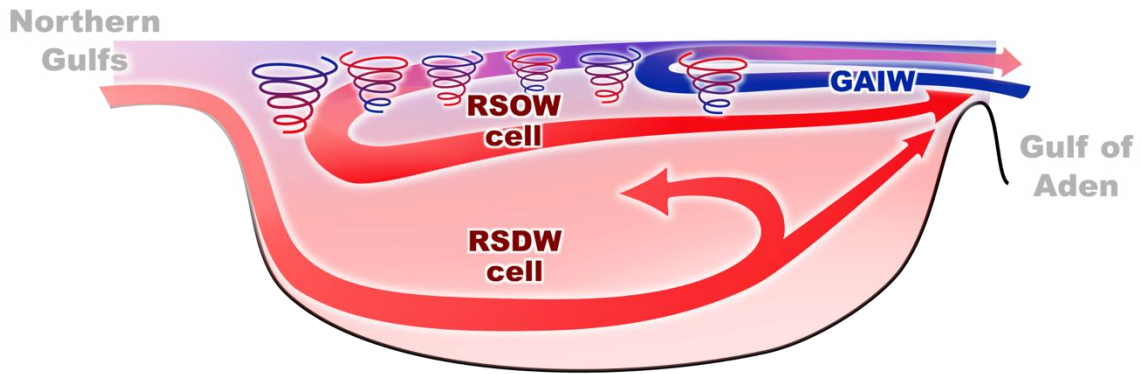
Figure 2. Schematic representation of the main thermohaline cells in the Red Sea circulation (Carvalho et al., 2018). Blue colors represent fresher waters while red colors saline and denser water masses. Mesoscale features, cyclonic and anti-cyclonic eddies, are represented by spirals. RSOW, RSDW and GAIW respectively stand the for Red Sea Outlflow Water, Red Sea Deep Water and Gulf of Aden Intrusion Water.

1001
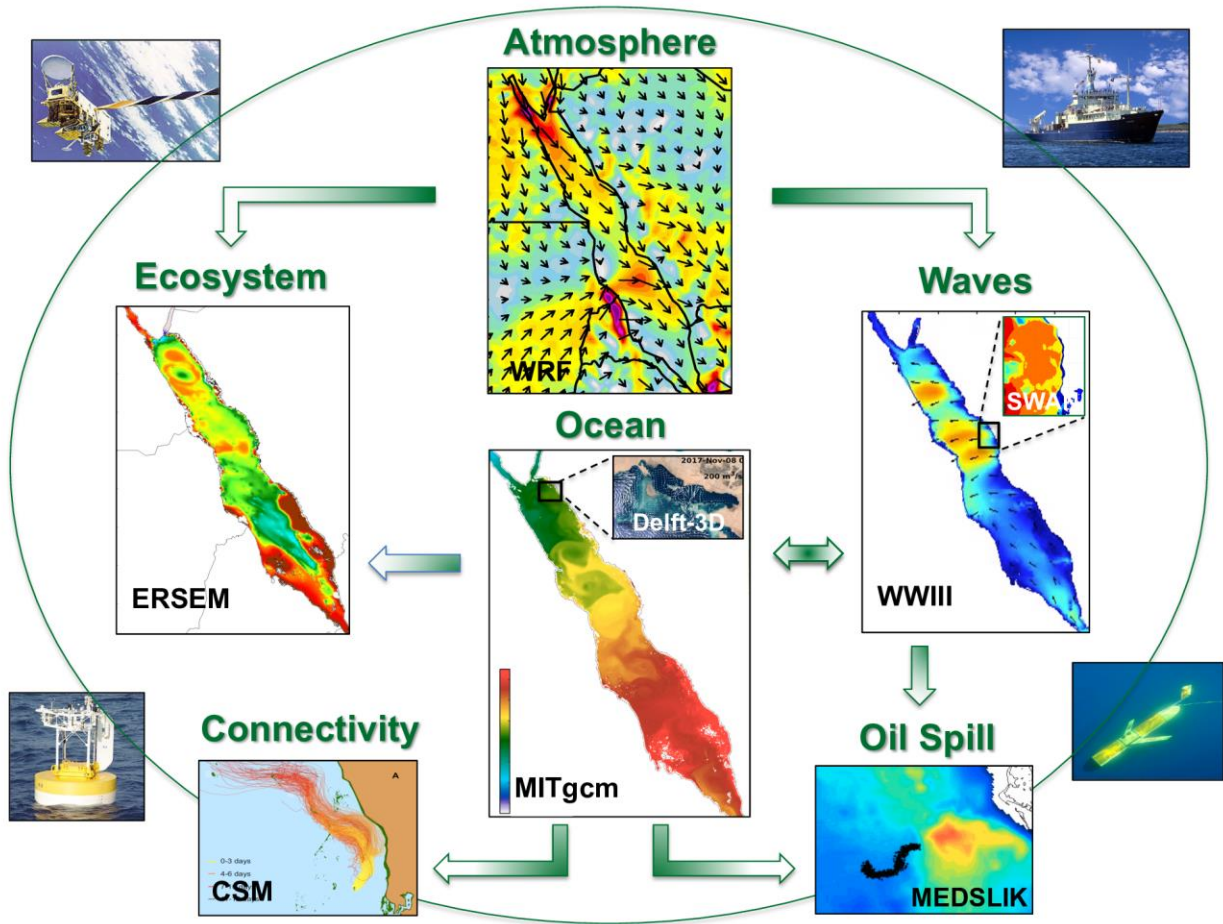
1002   Figure 3. Schematic illustration of the data-driven Red Sea modelling and prediction system

1003   (iReds-M1). Two-way arrows signify two-way coupling, and one-way arrows represent

1004   forcing of uncoupled components. The Atmosphere panel shows mean wind speeds during

1005   the month of July from 5 km WRF Red Sea reanalysis. The Ocean panel shows a sea

1006   surface temperature snapshot in September with the upper-corner subpanel displaying the

1007   volume transport in the upper layer of a high-resolution coastal nesting exercise in the

1008   NEOM region. The Ecosystem panel shows the simulated near-surface Chlorophyll-a

1009   during the winter-mixing period (January-March). The Waves panel shows a significant

1010   wave heights and mean wave directions snapshot in January with the upper-corner

1011   subpanel displaying the distribution of maximum significant wave heights estimated from

1012   a high-resolution nested coastal model long-run covering the KAEC region. The

1013   Connectivity and Oil spill panels show simulations of oil and virtual larvae trajectories

1014   released in the central Red Sea.

1015

52
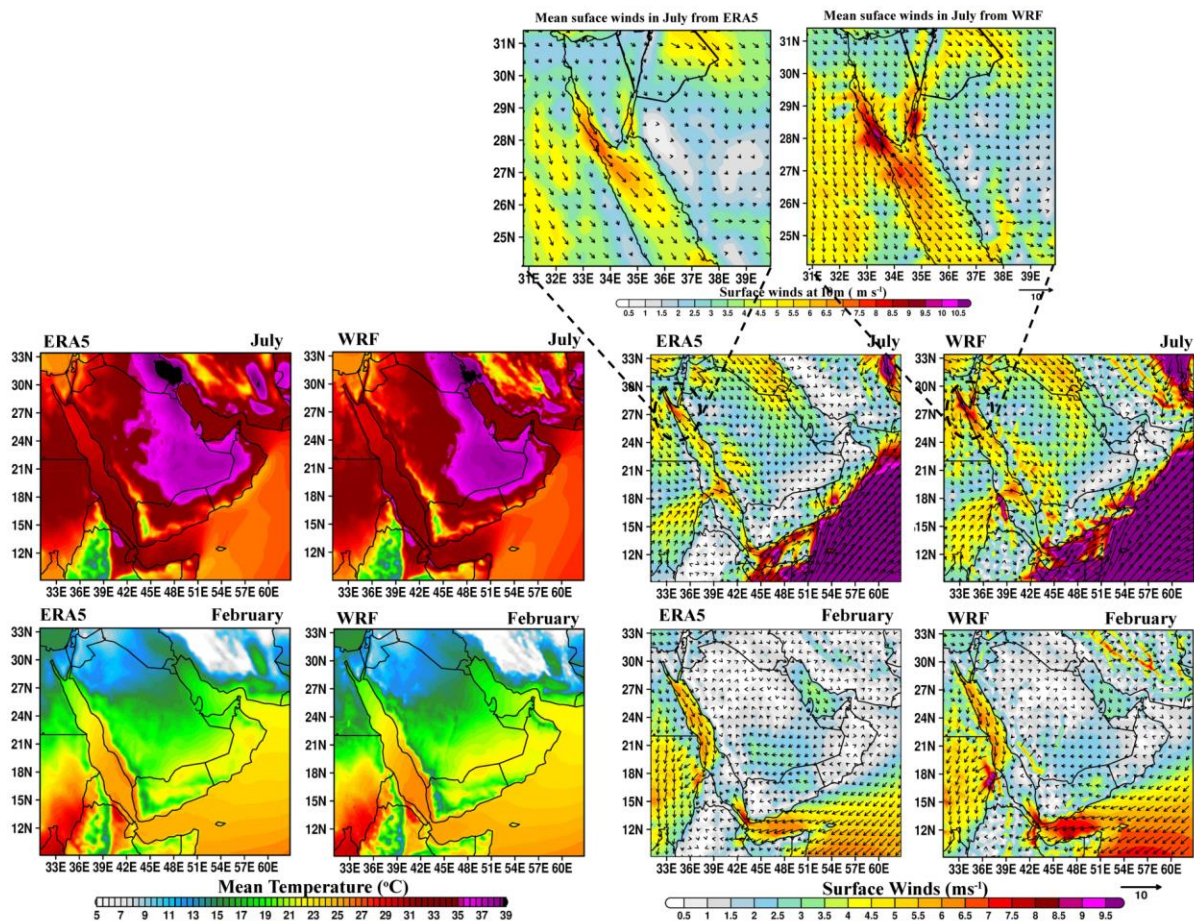
1016

1017   Figure 4. Lower panels show the spatial distribution of summer (July - top panels) and winter

1018   (February - bottom panels) months climatology of air temperature at 2 m height, and winds

1019   at 10 m height from the 5 km Red Sea reanalysis compared against ERA5 reanalysis. The

1020   Red Sea reanalysis reproduces well the main regional winds features in summer and winter,

1021   in good agreement with ERA5 reanalysis. The upper two panels zoom over the northern

1022   Red Sea region to emphasize the wind features captured by the high-resolution Red Sea

1023   reanalysis winds.

1024
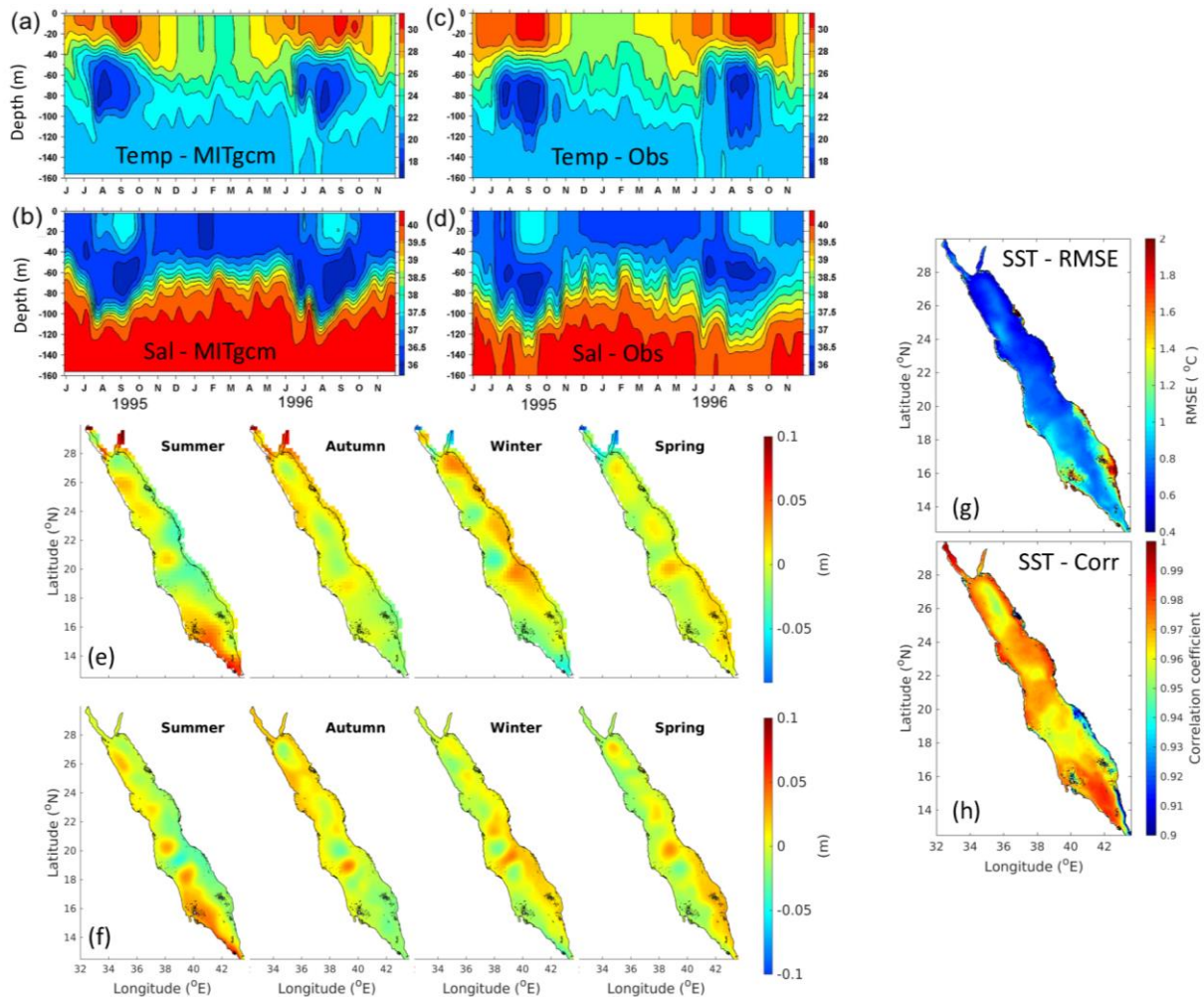
Figure 5. *Upper panel*s (a-d): Hovmöller diagrams (time versus water depth) of (a and c) temperature (°C) and (b and d) salinity (psu) at the Hanish Sill, from June 1995 to November 1996, after filtering with a 20- day low- pass filter. (a) and (b) show 400m resolution southern Red Sea MITgcm simulations taken from Xie et al. (2019) and (c) and (d) display in situ observations. *Lower panels* (e-f): Seasonal climatology of sea level anomaly derived from (e) satellite altimetry data (AVISO) and (f) 1 km MITgcm for the period 2001-2015, in summer (June-August), autumn (Sep-Nov), winter (Dec- Feb) and spring (March-May). *Right panels*: (g) RMSE and (h) correlation coefficient between satellite derived SST (OSTIA) and 1 km daily MITgcm SST, time averaged over the model

1035   simulation period 2001-2015. MITgcm successfully reproduces the main features of the

1036   general circulation of the Red Sea.

1037

1038

1039
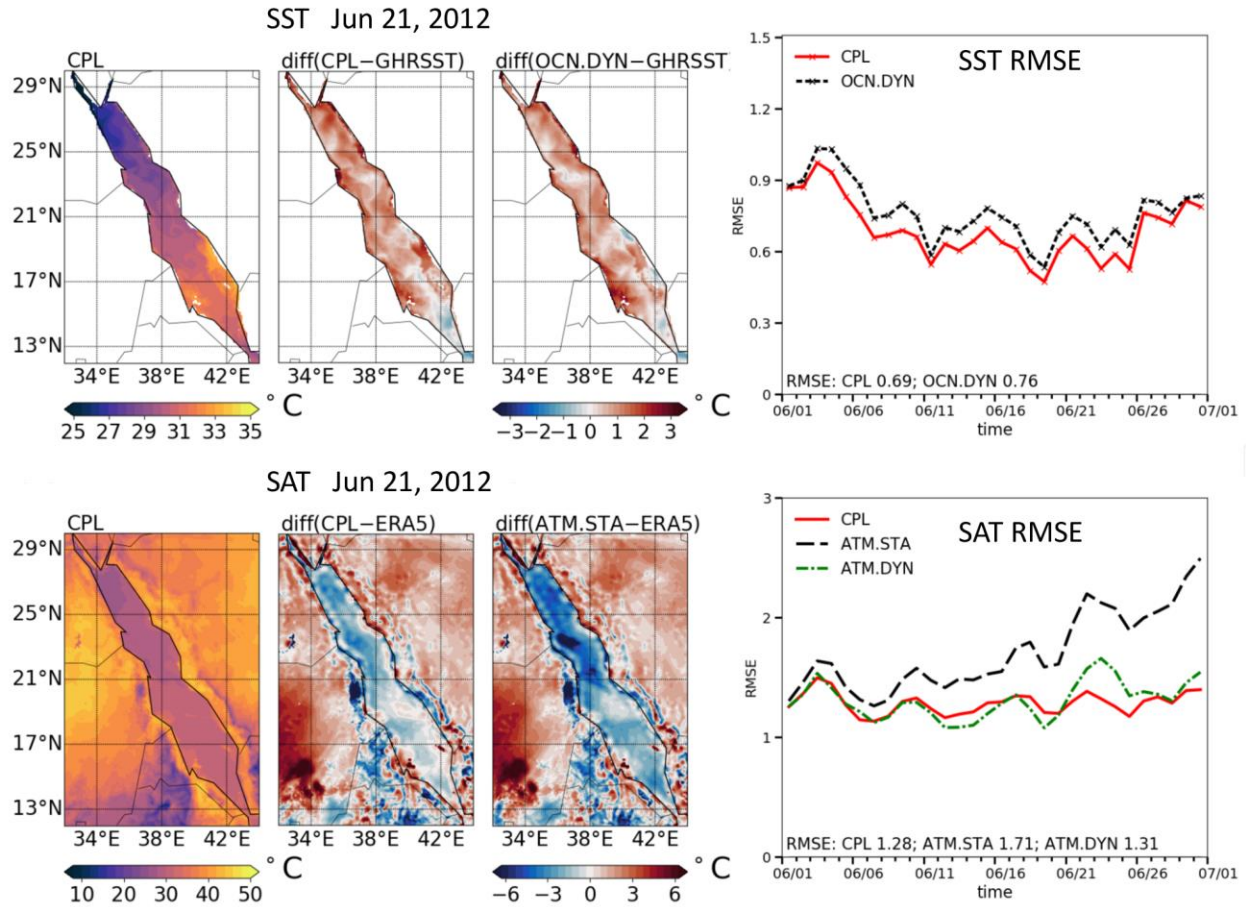
1040
1041
1042   Figure 6. Upper and lower panels respectively show validation results for sea surface temperature

1043   (SST) and surface air temperature (SAT) as simulated by the coupled SKRIPS model (Sun

1044   et al., 2019). CPL, OCN.DYN, ATM.STA, ATM.DYN denote the coupled WRF-MITgcm

1045   run, MITgcm-only driven by ERA5, WRF-only run driven by persistent HYCOM SST,

1046   WRF-only run driven by time-varying HYCOM SST, respectively. SST is compared

1047   against GHRSST and SAT against ERA5. The simulation initial time is 0000 UTC Jun 01

1048   2012 for all runs. Coupled and uncoupled runs well simulate SST and SAT in the Red Sea

1049   region with smaller RMSEs from the coupled simulation compared to the validation data.

1050
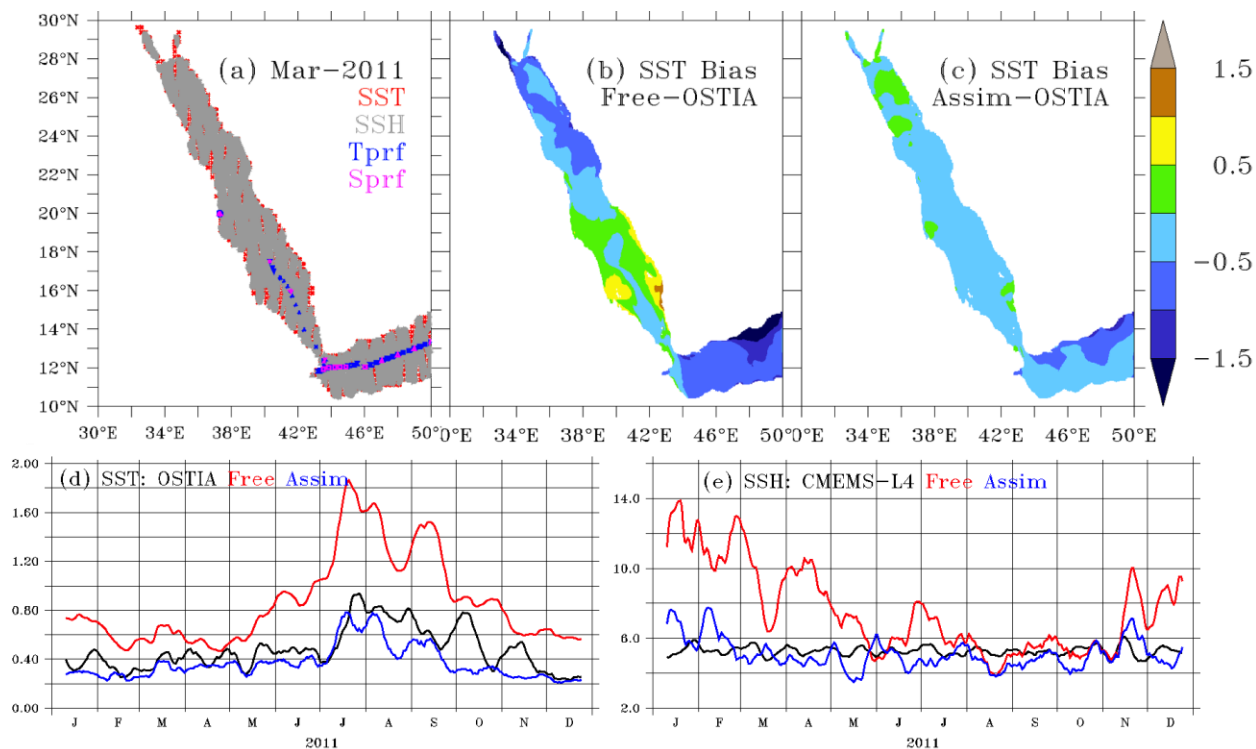
1051

1052   Figure 7. Impact of assimilation in the ensemble DART-MITgcm assimilation system. Panel (a)

1053   displays the spatial distribution of SST, SSH, and in-situ temperature and salinity observations

1054   that were assimilated in the DART-MITgcm ocean ensemble system during an arbitrary month

1055   (March 2011). The coverage of the regularly-spaced SST observations (red dots) is mostly

1056   masked by that of along-track SSH (grey dots) observations, which cover most of the Red Sea

1057   basin over a month period. Panels (b) and (c) respectively show the SST bias for free- and

1058   assimilative-model runs estimated over the period 1st March-31st December, 2011 with

1059   respect to OSTIA, a 5km resolution daily available interpolated level-4 gridded product

1060   generated by blending satellite and in situ observations of SST. Panels (d) and (e) respectively

1061   display time series of forecast RMSEs averaged over the model domain for SST (°C) and SSH

1062   (cm). Black, red and blue curves correspond to RMSEs of OSTIA for SST and CMEMS-L4

1063   for SSH (daily available at 25km resolution), and free- and assimilative-model runs,

1064   respectively.

57

1065
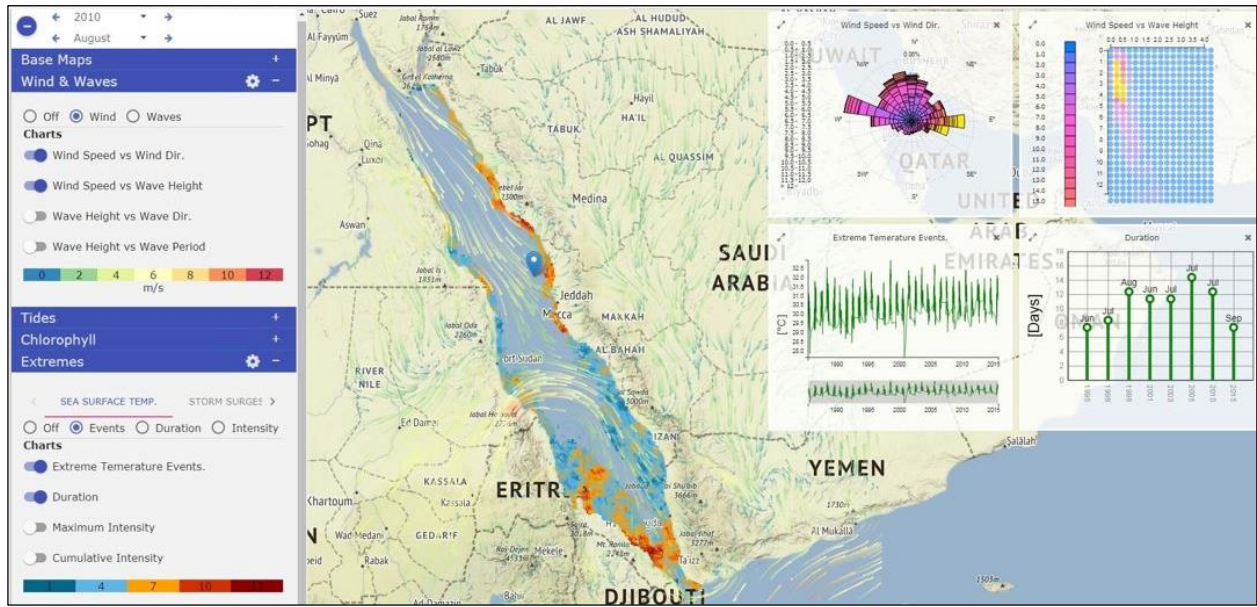
1066

1067

1068   Figure 8. The 'RedSeaAtlas' system showing overall wind patterns and statistics (at the dropped

1069   pin location, here north of Jeddah in the central Red Sea) of extreme temperature events in

1070   the Red Sea. Users can select any region to show more detailed information and associated

1071   attributes through different charts (Afzal et al., 2019).

1072

1073

1074

58
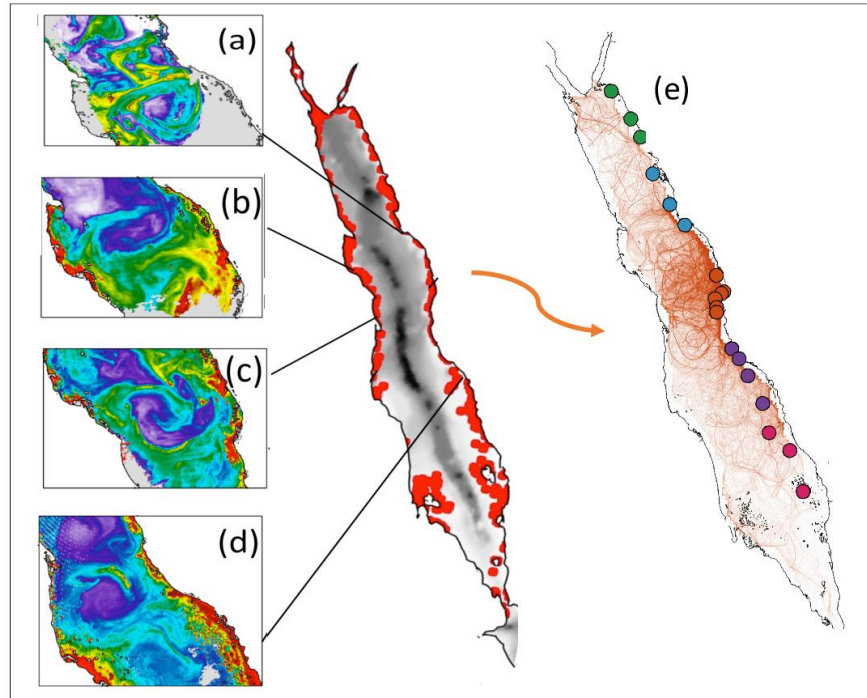
1075

1076   Figure 9. Remotely-sensed ocean colour observations portraying surface flow (eddies and

1077   currents) between coral reefs in the Red Sea. *Left panels* (a-d): Chlorophyll (mg/m3)

1078   patterns at different time periods (1-Jun-2010, 21-Jun-2009, 4-Mar-2006, and 13-Apr-

1079   2001) illustrating the impact of the basin-wide mesoscale variability on the basin

1080   productivity. The central map depicts sea-floor elevation and the position of coral reefs

1081   (red circles) in the Red Sea (coral reef positions were acquired from: Global Distribution

1082   of Coral Reefs, 2010). (e) Simulated particle dispersion trajectories forming pathways of

1083   connectivity in the Red Sea. Particles were released from the locations of the coral reefs

1084   along the east coast of the central Red Sea. The different colours denote each of the five

1085   different Red Sea provinces (Raitsos et al., 2013). The panel suggests basin-wide

1086   connectivity with the central Red Sea driven by mesoscale activity, except for the southern

1087   Red Sea which connects more with the Gulf of Aden (Raitsos et al., 2017; Wang et al.,

1088   2019).

1089

1090
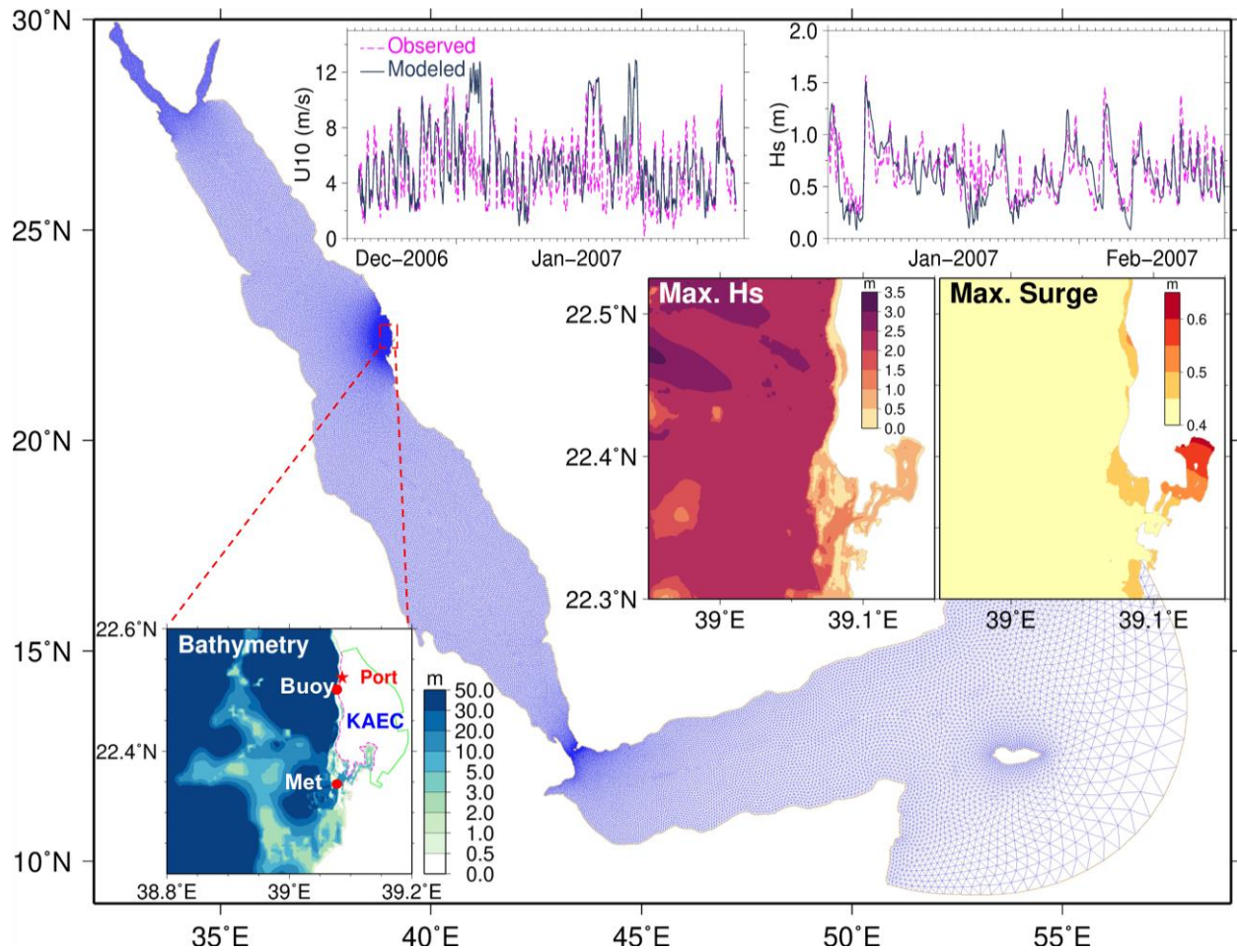
1091

1092   Figure 10. Coupled ADCIRC+SWAN model domain used for estimating extreme wave heights

1093   and water levels along the KAEC coastline. The unstructured grid resolution varies from

1094   60 km near the boundary in the Arabian Sea to 60 m near the KAEC coastline. The

1095   bathymetry of the KAEC and maximum of significant wave heights and water levels from

1096   30-year simulations are also shown in inset images. The model-data comparisons at the

1097   locations indicated in the Bathymetry plot (by Met for winds and Buoy for waves) suggest

1098   a good agreement between the model simulations and the measurements.

1099
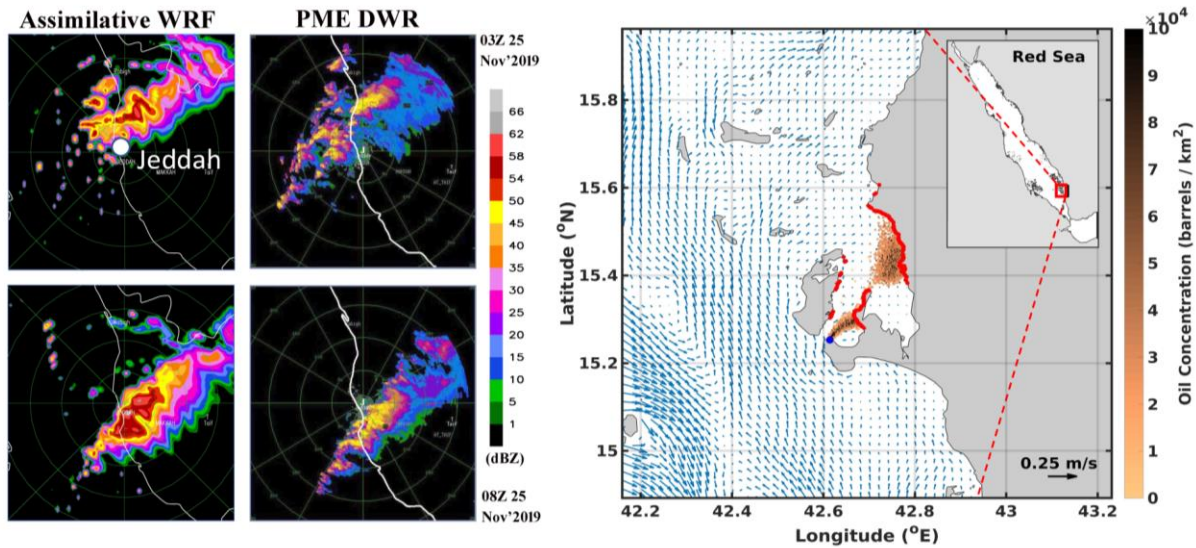
1100

1101   Figure 11. (a) Evolution of reflectivity as predicted by WRF with assimilation of conventional and

1102   satellite radiance data against PME DWR data during Jeddah extreme rainfall event at 0300

1103   UTC, and 0800 UTC on 25 November 2009 (Viswanadhapalli et al., 2016). (b)

1104   Concentration of oil (in barrels/km2) after 14 days of spill from the tanker location marked

1105   by the blue dot. Red dots indicate beached spill locations. The investigated region is

1106   indicated by the red box in the inserted Red Sea basin panel.

1107